POLITECNICO
DI TORINO

The LEAF system and gamma detection applications in CROCUS

Master of Energy and Nuclear Engineering

Master's Thesis
by

Tom Mager

realized at the
Faculty of Sciences de Base
Laboratory of Reactor Physics and Systems Behaviour (LRS)
École Polytechnique Fédérale de Lausanne

4th February 2020

Academic advisor:	Sandra Dulla Politecnico di Torino
Supervisor:	Dr. Vincent Lamirand PSI & EPFL Oskari Pakari EPFL

LABORATORY FOR REACTOR PHYSICS
AND SYSTEMS BEHAVIOUR

Contents

List of Figures

List of Tables

Chapter 1

Introduction

The work at hand is the result of a master's thesis project in the winter semester of 2019-2020 at the Laboratory for Reactor Physics and Systems Behaviour of the Swiss Federal Institute of Technology Lausanne (LRS-EPFL). The overall goal of the project is to better understand how gammas are produced, how they behave in nuclear reactors, and more specifically in CROCUS. For this purpose, the LEAF system (The Large Energy-resolving detection Array for Fission Gammas) was calibrated, characterized and used for three applications in CROCUS:

- In-core gamma spectra measurements.
- Delayed gamma fraction determination.
- Gamma noise measurements.

The motivations for each of these focuses are briefly introduced hereafter and will be thoroughly presented in the three following chapters.
In a nuclear reactor, gamma-rays are ubiquitous and arise from fissions, decays following activation of fission products or from capture processes occurring in fuel or in reactor components. Gamma-rays have a major contribution to the heating of the reactor structures and to the surrounding dose rate. Accurately characterizing the gamma field in nuclear reactors is therefore of strong interest for core operation and safety concerns. First, the measurements of in-core spectra with the LEAF system may allow the identification and quantification of isotopes presents in CROCUS. Essential to dose estimates or burn up calculations, these spectra compared to code predictions could help code validations and to identify the nuclear processes yet to model in coupled neutron-gamma transport codes, such as delayed processes. Then, the delayed gamma determination of prompt to delayed gamma ratios in CROCUS could enable the validation of delayed gamma transport codes, aiming at a full description of the gamma field in nuclear reactors. Furthermore, since a substantial part of gamma-rays are side products from fission chains originated by neutrons, gamma noise should, as neutron noise, provide the temporal information needed to determine reactor kinetic parameters. The gammas higher mean free path compared to neutrons would allow for even less intrusive detector positioning than classic neutron noise experiments.

Chapter 2 gives a full characterisation of the LEAF detectors including energy and efficiency calibrations. Chapter 3 presents the gamma field characterisation performed in CROCUS from the first in-core gamma spectra to the delayed gamma fraction determination. Chapter 4 introduces the neutron and gamma correlations measurements conducted in CROCUS. Chapter 5 provides an overview of the project and an outlook to future projects in CROCUS regarding gamma field investigations and branching noise analysis using gammas.

Chapter 2

The LEAF System for the CROCUS Reactor

The contribution of gamma radiation to the heating and dose of nuclear reactors components is significant. Thus, measuring gamma rays is of major interest to experimentally validate computed spectra, estimate doses or characterize the prompt to delayed gamma ratios. In order to collect such experimental data, gamma detection capabilities were added to the CROCUS reactor facility at the Swiss Federal Institute of Technology Lausanne (EPFL). In this chapter we introduce first CROCUS and then in detail the new LEAF system, which is composed of two large Bismuth Germanate (BGO) and two Cerium Bromide ($CeBr_3$) scintillators, and we provide their energy and efficiency calibration.

2.1 The CROCUS reactor

CROCUS is a zero power reactor situated on the EPFL campus. With its maximum allowed power of 100 W, dose rates inside the shielding are acceptably low after shutdown for flexible use for teaching and research. Figures 2.1a and 2.1b depict the reactor, with the approximately cylindrical active core being $\sim 60\,\text{cm}$ in diameter and $\sim 1\,\text{m}$ high. Its fuel is composed of two regions: an inner uranium oxide region with 336 rods enriched to 1.806% and an outer uranium metal region with 176 rods enriched to 0.947%. A vessel of 1.3 m diameter is the outer boundary holding the moderator and reflector, demineralised light water. The water level, controlled via a spillway, and optionally B_4C control rods are used to control criticality.

2.2 Gamma-ray interactions and detection principles

Gamma radiation arises from radioactive decay of atomic nuclei. The detection of uncharged gamma particles, unlike charged particles, as alphas or betas, which directly produce an electrical signal in the detector material by ionization or excitation, relies on radiation-material interaction involving energy transfers to electrons. Photoelectric effect,

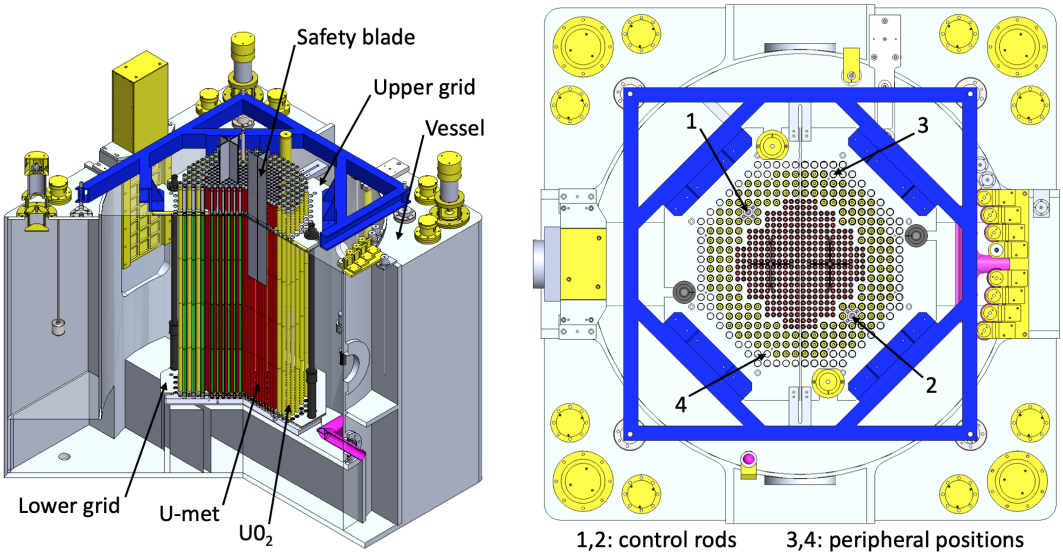

(a) Cross-section **(b)**

Figure 2.1: Schematics of the CROCUS. (a) Reactor vessel with its internal structures. The inner part of the fuel consists of uranium dioxide rods while the outer part is uranium metal rods. Fuel rods are being held by two grids and lie on a base plate. (b) Top-view with highlighted control rod and peripheral positions used for detector positioning.

Compton scattering or Pair production ([2], Chap.2) are predominant in the energy range of interest. These charged electrons deposit their energy inside the detector material by ionization or excitation. The deposited energy is then collected to produce an electrical signal. The collection process depends on the detector type.

This section gives an overview of the most commonly used gamma detector types considered for this work and a general description of signal processing for different detection modes.

2.2.1 Gamma detectors for spectrometry

The gamma absorption cross-section being proportional to the material atomic number Z and to the density, the absorption coefficient of gamma particles in gases is very low so gaseous detectors will not be described. Hence, gamma radiation detectors for spectrometry are mostly made of solid materials in order to efficiently absorb gamma rays. Then depending on the material characteristics, different methods to collect the energy deposited can be used.

Semiconductors Semiconductor materials as insulators have full valence bands, contrary to metals. However, semiconductors band gap is much smaller than insulator's (about 1eV against tens of eV) which may allow excited electrons to be promoted from the valence to the conduction band, leaving a vacancy. This vacancy can then be filled by another electron, leaving another vacancy deeper in the occupied bands. If an external electrical

field is applied to the material, the electron seems to move toward the cathode and the "hole" toward the anode, creating an electrical signal. Since gamma ray energies are a lot larger than the energy gap, interactions within the material will rise electrons from deep occupied bands and produce cascades of electron-hole pairs, which actual number will be directly proportional to the incident energy. Although semiconductors are providing a direct mean to collect electron-hole pairs and produce an electrical signal, not so many of them have a low gap and a good electron-hole mobility, are available in high purity at reasonable cost, and are large enough in volume in order to absorb a significant portion of gammas. Taking into account these considerations, Silicon and Germanium are the most used materials for spectrometry purposes.

Scintillators Scintillators may be inorganic crystals, organic plastics and liquids, gas or glasses. In inorganic crystals, gamma-ray energy conversion into primary electrons follows the same principles as in semiconductors, however the collection process differs as the energy from the incident radiation is converted into visible light. When struck by an incident radiation, electrons of the crystal are excited into the conduction band. These excited electron will then de-excite down to the valence band by emitting photons. This emission can be direct in case of fluorescence -only $\simeq$10 ns delay from the time of the energy deposition to the emission of light- or retarded through phosphorescence -the electron being trapped into energy levels which prohibit direct de-excitation. If the emitted radiation is within visible wavelengths, it can then for instance be detected by a photomultiplier tube (PMT). As illustrated in Figure 2.2, the scintillation photon strikes the photocathode which, as a result, emits a photoelectron. Then, a series of dynodes is amplifying the signal by electrostatically focusing the photoelectrons. The amplified signal is finally collected at the anode.

In order to allow gamma ray spectroscopy, the scintillator material must ideally have the following properties ([2], Chap.10):

- a large enough light yield: number of secondary photons emitted by the de-excitation of electrons per unit of energy deposited;
- high stopping power for gamma radiation;
- a linear response with energy;
- transparent to the emitted light;
- short decay time of the excited state to allow high count rates;
- availability at reasonable cost;
- refractive index close to glass to allow coupling to photomultipliers.

Inorganic crystals such as sodium iodide (NaI), caesium iodide (CsI), bismuth germanate (BGO) or cerium bromide ($CeBr_3$) exhibit these properties.

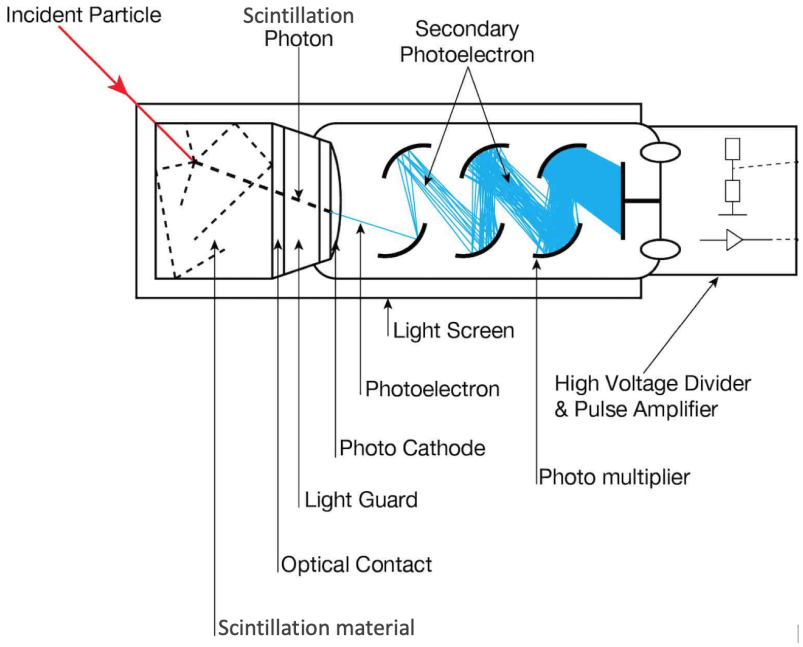

Figure 2.2: Concept of a scintillator detector. A scintillation crystal is optically coupled to a photomultiplier tube, connected to a preamplifier. Wiki.org Licence CC BY-SA 3.0

2.2.2 Electronics for signal processing

A detector can be used for spectroscopy as long as the output electrical signal is proportional to the energy of the incident particle. The electronic system aims at collecting the energy deposited, turning it into an amplified and shaped voltage pulse while the acquisition system sorts and stores the information ([2], Chap.4). In a scintillation detector, the PMT is converting the quantity of light emitted in the crystal into a pulse of current at the anode. This pulse is converted from current into a voltage pulse thanks to a connected pre-amplifier which consists in a voltage divider (Figure 2.2). Scintillator, photomultiplier and preamplifier can be combined to form a compact assembly. The resulting voltage pulse is then amplified by a millivolt-to-volt amplifier. The fast rise time of scintillation pulses constraints the amplifier time constant to stand within 0.2 to 2 μs.

2.3 The LEAF system

Scintillators were chosen for their flexible use, reasonable price, and nonetheless high efficiency when compared to semiconductor based detectors. Indeed, scintillators are more convenient to be used in limited space since they do not need cooling to cryogenic temperatures as HPGe do, and they present a higher radiation hardness which is a valuable advantage for reactor applications. In total, four detectors were acquired to allow for symmetric placement of the system in and around the core. In this section we introduce the respective detectors in detail and present their characteristics.

2.3.1 The LEAF detectors

Cerium Bromide ($CeBr_3$) The control rod guide tubes of CROCUS, which can be seen in Figure 2.1b, offer a suitable location for in-core measurements. Due to the high photon flux in the tubes, a quickly decaying scintillator was required not to be limited by dead time issues. Cerium Bromide (CeBr3) detectors (Figure 2.3), with a decay time of 20 ns and a light yield of 45k photons/MeV at a density of 5.2 g/cm^3 [3], has been estimated to be adequate for CROCUS. This relatively new material presents better or as good results as Lanthanum halides, which were considered to be the reference, in terms of resolution, sensitivity and linearity of response [4]. CeBr3 scintillators can be used in a wide range of applications, such as isotopic identification and coincidence counting.

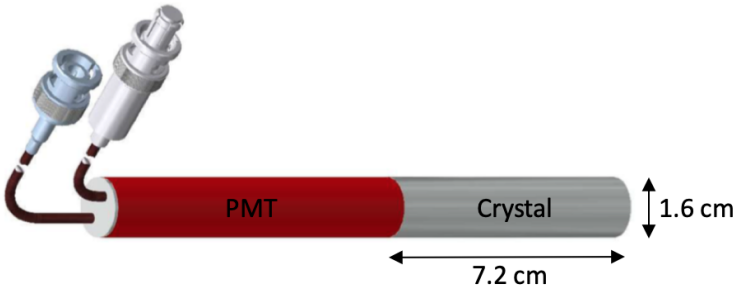

Figure 2.3: Sketch of a CeBr3. Technical drawings are in Appendix A.

Bismuth Germanate (BGO) For ex-core applications a material with high efficiency was required because of the expected flux drop, and with the intent to detect gamma-rays up to 10 MeV, which is not possible with $CeBr_3$ due to their small size.. Bismuth Germanate (BGO) detectors, presented Figure 2.4 -with a decay time of 300 ns and a yield of 9k photons/MeV [5]- have been selected.

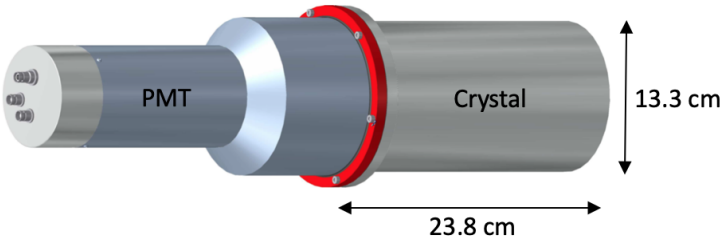

Figure 2.4: Sketch of a BGO detector. Technical drawings are in Appendix A.

2.3.2 The electronics of the LEAF system

The high voltage supply and photomultiplier (PMT) signal treatment was handled by the fully integrated DSA-LX [6] that theoretically allow for MHz count rates to be treated. These very compact instruments integrate both amplifying and digitization of the signal, in addition to the high voltage supply. For spectroscopy purposes the output digitized signal is operated through CANBERRA's Genie 2000 software on the "LEAF PC", while for Noise analysis, the amplified signal is directly transmitted to the "PSI Noise PC". This is summarized on Figure 2.5.

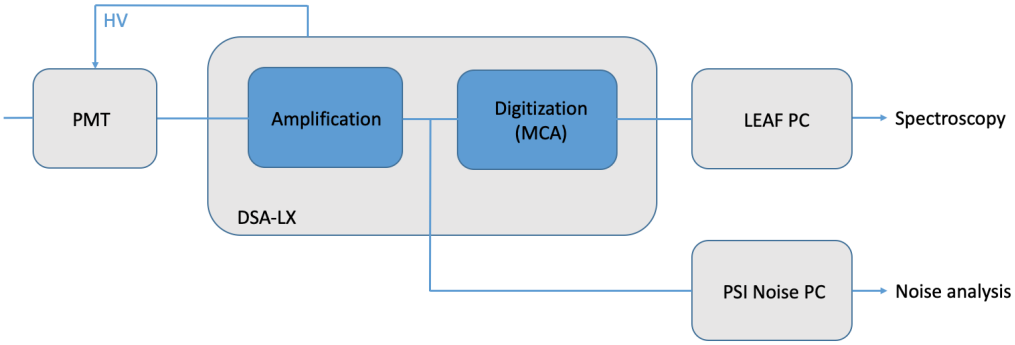

Figure 2.5: Schematic of the electronics used for the LEAF system detection signal processing, either for gamma spectroscopy or for time dependant counting.

2.4 Energy calibration

All four detectors were calibrated using standard Eu-152 sources. No shielding was used and the sources were placed in contact with the crystals. The resulting spectra are displayed in Figures 2.6 and 2.7. The DSA-LX's settings were as follows, for all experiments:

- Rise time of $0.2\mu s$, $0.0\mu s$ flat top.
- -610 V and -1260 V of HV for the $CeBr_3$ and BGO PMTs, respectively.
- Lower level discrimination at 0.5% of the maximum channel (2^{14}).
- Coarse gain of 6.4 for all detectors.

The energy calibration for the $CeBr_3$ is presented Figure 2.6. In addition to the Eu-152 measurements, a Co-60 source was needed to help in the peak distinction for the BGO (Figure 2.7), due to its comparatively poorer resolution. The final linear calibrations are shown in Figures B.1 and B.2 from Appendix B, along with the full width half maximum as a function of the energy.

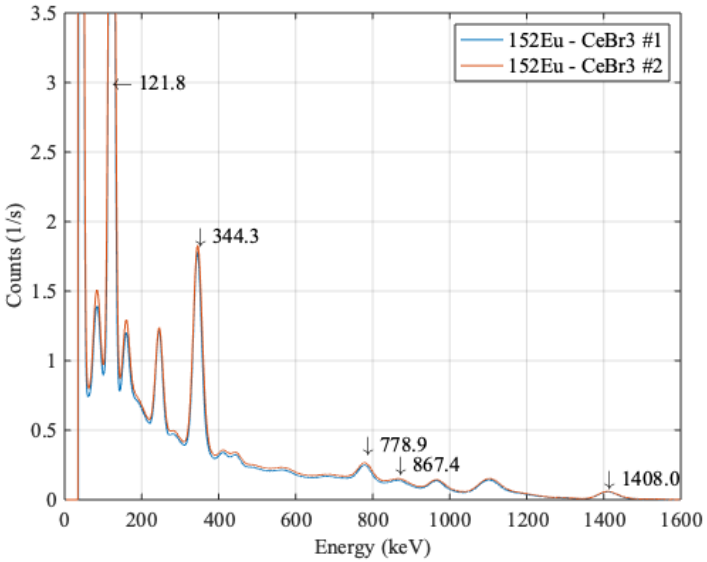

Figure 2.6: Eu-152 spectra acquired with both $CeBr_3$ detectors using DSA-LX for HV supply and signal treatment.

2.5 Efficiency calibration

The efficiency calibration of a detector is linking the peak area at a particular energy in the spectrum to the incoming flux of particles. Calibrating a detector in efficiency, in order to scale the spectra and characterised the source, is prior to any isotope quantification or activity measurement.

2.5.1 Experimental setups

The efficiency strongly relies on the geometrical setup of source and detector, but also on the internal conversion process of the detector. Therefore, the experimental setup should be as precise as possible to allow for an accurate modelling. The Eu-152 sources was hanged in front of the detector at several distances and no shielding was used. The gamma background was removed from the spectra but not additional scattering contributions. The setups are sketched on Appendix C. Both the geometry and materials involved in the experiments have been carefully chosen in order to be easily implemented and simulated on codes, as Serpent [7], allowing for photon transport.

2.5.2 Monte Carlo simulation using Serpent 2

Serpent is a Monte Carlo particle transport code developed at VTT Technical Research centre of Finland [7]. It allows for traditional reactor physics applications such as criticality calculations or fuel cycle studies, multi-physics simulations or neutron and photon transport simulations.

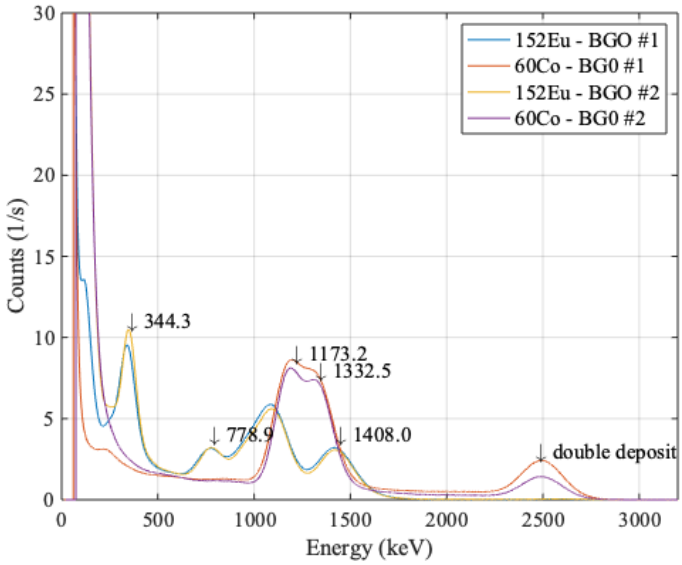

Figure 2.7: Eu-152 and Co-60 spectra acquired with both BGO detectors using DSA-LX for HV supply and signal treatment.

Both detectors geometries (Appendix D) have been modelled using the simulation code Serpent 2. The source position and isotope are parameters to be tuned. Serpent allows photons transport [8] from the source to the detector and photons interactions in the crystal to be counted thanks to the "det -27" tally [9]. Knowing the energy of the incident gamma-rays and the energy deposited in the detector crystal, the geometric efficiency curves of the studied detectors displayed in Figure 2.8 could be retrieved. As expected, the farther the source the lower the efficiency.

2.5.3 Theoretical discussion on scintillators intrinsic efficiency

A detector absolute efficiency ϵ_{abs} relates the number of gamma-rays emitted by the source to the number of counts detected anywhere in the spectrum([2], Chap 7). It can be divided into two terms: the intrinsic ϵ_{int} and the geometric ϵ_{geom} efficiencies (Equation 2.1) . The geometric efficiency usually relates the number of gamma-rays emitted by the source to the number of gamma-rays entering the detector crystal. However, for simulation purposes the geometric efficiency is defined here as the number of gamma-rays emitted by the source to the number of gamma-rays which deposit energy in the crystal.

$$\epsilon_{abs} = \frac{Counts}{Source} = \epsilon_{int} \cdot \epsilon_{geom} = \frac{Counts}{N_1} \cdot \frac{N1}{Source} \tag{2.1}$$

where:

- $Counts$: Number of counts registered in the acquisition system.

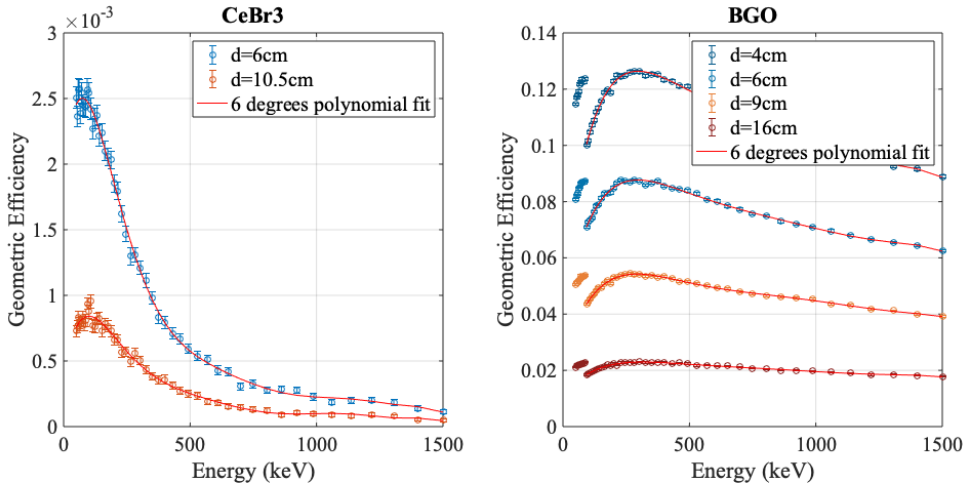

Figure 2.8: Simulated geometric efficiency with Serpent for $CeBr_3$ and BGO at several source distances. The discontinuity on the right-hand side plot at 90 keV corresponds to the K-edge of Bismuth.

- *Source*: Number of gammas emitted at the source.
- N_1: Number of primary gammas interacting in the crystal.

The defined efficiency is calculated directly from the analysis of the spectra obtained through the experiments, using Equation 2.2:

$$\epsilon_{abs}(E) = \frac{N(E)}{\Delta t \cdot A \cdot P_E} \tag{2.2}$$

where:

- $N(E)$: Net peak area at the energy E, obtained from the measured spectrum.
- P_E: Probability that the gamma is emitted with an energy E.
- A: Activity of the source at the time of the experiment.
- Δt: Measurement time.

The geometric term is determined thanks to Serpent simulations with the "det -27" tally to get a spectrum of pulse heights. The intrinsic efficiency term depends on the technology of each detector. In the case of a scintillation detector (Figure 2.2), it represents how the energy deposited in the crystal by gamma interactions is emitted to the photocathode and, then, transmitted through the PMT.

The intrinsic efficiency, which links the number of primary gammas interacting in the crystal to the number of counts registered in the acquisition system, depends on the crystal

scintillation processes and on the PMT design. A thorough derivation of this term is done in Appendix C and results in the following expression:

$$\epsilon_{int} = \epsilon_{PMT} \cdot \eta \cdot \epsilon_{crystal} \cdot \frac{h\bar{\nu_1}}{h\bar{\nu_2}} \tag{2.3}$$

where $\epsilon_{crystal}$ is the scintillation efficiency, η represents the fraction of scintillation photons reaching the photocathode and ϵ_{PMT} is the PMT intrinsic efficiency. $h\bar{\nu_1}$ is the mean absorbed energy in the crystal per incident gamma and $\bar{\nu_2}$ is the mean emitted energy per scintillation photon.

Results

Cerium Bromide The efficiency calibration of the $CeBr_3$ detectors was realised with an Eu-152 source placed at distance $d_1 = 6$ cm and $d_2 = 10.5$ cm. The gamma peaks at $E_1 = 121.8\ keV$, $E_2 = 344.3\ keV$, $E_3 = 778.9\ keV$, $E_4 = 964.1\ keV$ and $E_5 = 1408\ keV$, clearly present in the measured spectra Figure 2.6, were used to determine the respective absolute efficiencies $\epsilon_{abs}(E_i)$ for both CeBr3 detectors. The corresponding geometric efficiencies were obtained thanks to the Serpent simulations.

In light of Equation 2.3, a constant value for ϵ_{int}, is considered:

$$\epsilon_{int}^{detector}(E) = \frac{1}{2}\left[\left(\frac{1}{5}\sum_{i=1}^{5}\frac{\epsilon_{abs}^{i\ \ detector}}{\epsilon_{geom}^{i}}\right)_{d_1} + \left(\frac{1}{5}\sum_{i=1}^{5}\frac{\epsilon_{abs}^{i\ \ detector}}{\epsilon_{geom}^{i}}\right)_{d_2}\right] \tag{2.4}$$

where for each detector, the ratio between the measured absolute efficiency and the simulated geometric one is made, at each of the five energy considered, for both source distances d_1 and d_2. Then, the mean value between the intrinsic efficiencies obtained at these different source distances is taken. The results are given in Table 2.1.

Table 2.1: Intrinsic efficiency values for $CeBr_3$ detectors, in counts per gammas interacting in the crystal.

Detector Id	Intrinsic efficiency
$CeBr_3$ #1	0.09034(1)
$CeBr_3$ #2	0.12172(1)

The measured absolute efficiencies, scaled with the intrinsic efficiency values from Table 2.1, are compared to the Serpent simulated geometric efficiency curves obtained in Subsection 2.5.2. The results are displayed in the C/E plots Figure 2.9. Judging from these plots, the measured absolute efficiencies can be correctly scaled by constant intrinsic efficiencies into the geometric efficiency curves fit 10% confidence bounds. We observe some discrepancies

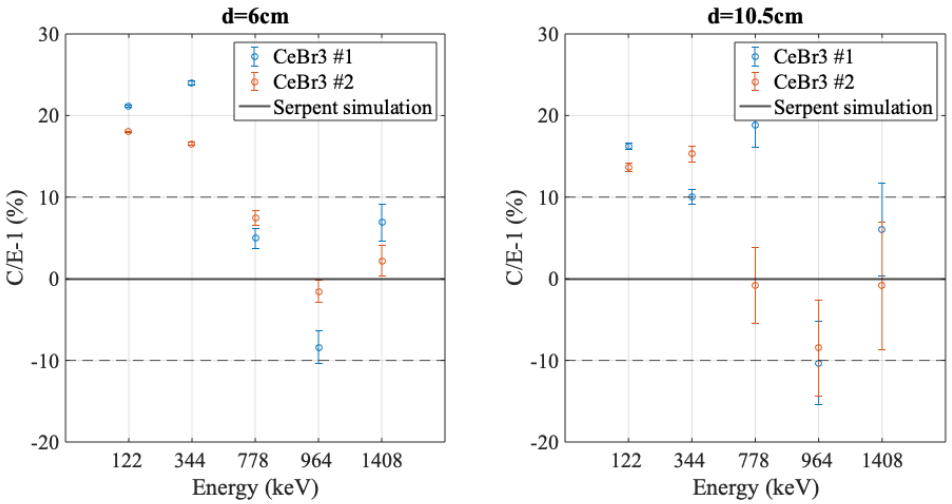

Figure 2.9: C/E plots for $CeBr_3$ efficiencies. Measured absolute efficiencies scaled with constant intrinsic efficiencies are compared to simulated geometric efficiencies.

at low energy which can be explained either by a high sensitivity of $CeBr_3$ to X-rays or by an important electronic noise contribution to the low-energy background. X-rays events or electronic induced counts may add up to the gamma peaks in the measured spectrum and lead to an overestimation of the ϵ_{abs} values.

From intrinsic efficiency values from Table 2.1 and from the crystal efficiency estimated before, we can deduce the PMT efficiencies in Table 2.2 (PMT efficiencies ate there including the fraction η). It appears that more losses occur in the $CeBr_3$ #1 conversion process than in the #2.

Table 2.2: PMT efficiency values for 91 and 92 $CeBr_3$ detectors, in counts per scintillation photons reaching the PMT's photocathode.

Detector Id	PMT efficiency
$CeBr_3$ #1	0.64(1)
$CeBr_3$ #2	0.86(1)

Bismuth Germanate The efficiency calibration was first tried with an Eu-152 source but the resolution of BGO detectors does not permit to clearly distinguish the Eu-152 gamma rays. Single peak (n,γ) reactions from gold and indium samples were used to avoid the resolution obstacle, however, although measured absolute efficiencies show consistency with respect to source distance and gamma-ray energy, a scaling with constant intrinsic efficiencies was not possible. According to the results of this investigation, which are fully presented in Appendix F, the theoretical splitting of the absolute efficiency from 2.3 seems not to be appropriate for large scintillation crystal where some energy dependent effects

must lie under the conversion process. As a result, BGO can not be used yet for applications needing a quantification of the gamma source, such as dose calculations, but they can still be used for isotopes identification (cf. Chapter 3) and noise measurements (cf. Chapter 4).

2.6 In-core efficiency calibration

The LEAF setup was acquired for in-core spectroscopy purposes. In order to quantify the isotopes identified in the in-core spectra, in-core efficiency calibrations are also needed. The previous section provides us with the intrinsic efficiencies of the LEAF detectors present in core ($CeBr_3$ in control rod positions), thus a geometric efficiency for these detectors must be calculated.

2.6.1 LEAF detectors in core modeling

One $CeBr_3$ detector has been added to the CROCUS Serpent geometry (see Figure 2.10). As control rod tubes are symmetrically positioned around the core centre, from the behaviour of one detector we will be able to assess for both detectors. Since the BGO detectors are positioned outside the main vessel, to get enough gamma-rays to reach the crystal would require a population of several billions of particles per simulation batch. Considering the poor resolution of BGO compared to $CeBr_3$ detectors, and the potentially high computation time induced by ex-vessel BGO simulations, the BGO efficiency curves in CROCUS will not be produced.

2.6.2 CROCUS gamma source evaluation

CROCUS can be operated at critical but also at several subcritical states with water level. Each core configuration corresponds to a different neutron flux and, as a result, to a different gamma source. In order to accurately determine the quantity of isotopes present in CROCUS, the efficiency curves produced by Serpent simulations should match the operation levels at which the spectra would be acquired. Although the gamma source is unknown in CROCUS, it can be inferred from the fission locations after a converged external source calculation for subcritical levels and from a standard k-static simulation at critical. Then, using the energy deposition det -27 tally from Serpent [8] and the same procedure as for the source calibrations detailed in the previous chapter, geometric efficiency curves, as in Figure 2.11, have been produced.

These computed geometric efficiency curves can be scaled by the intrinsic efficiencies of $CeBr_3$ detectors, which have been previously determined with the source calibrations. The gamma source for each CROCUS configuration can than be inferred from the resulting geometric efficiencies and the in-core spectra presented in the next chapter.

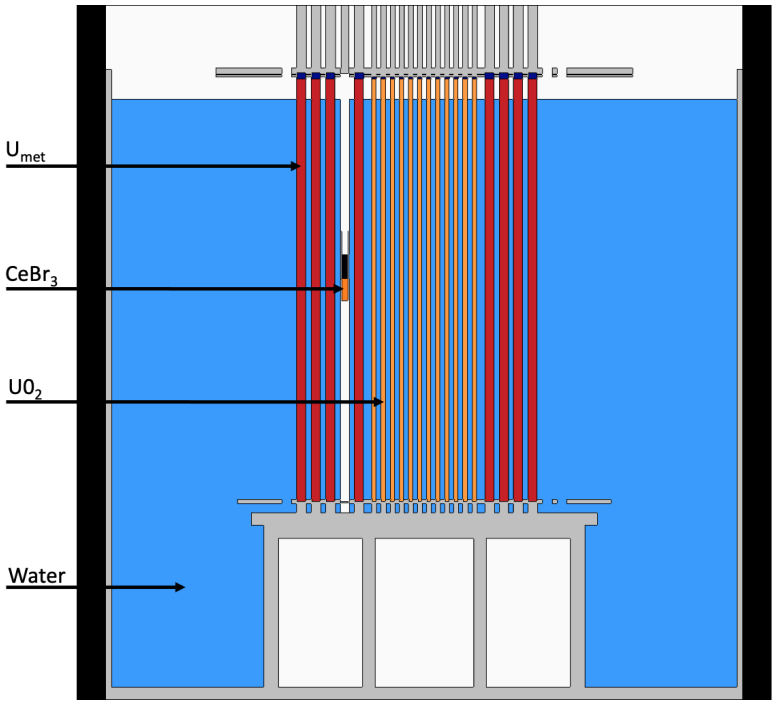

Figure 2.10: Serpent modelling section sketch of a $CeBr_3$ scintillator in a CROCUS control rod tube.

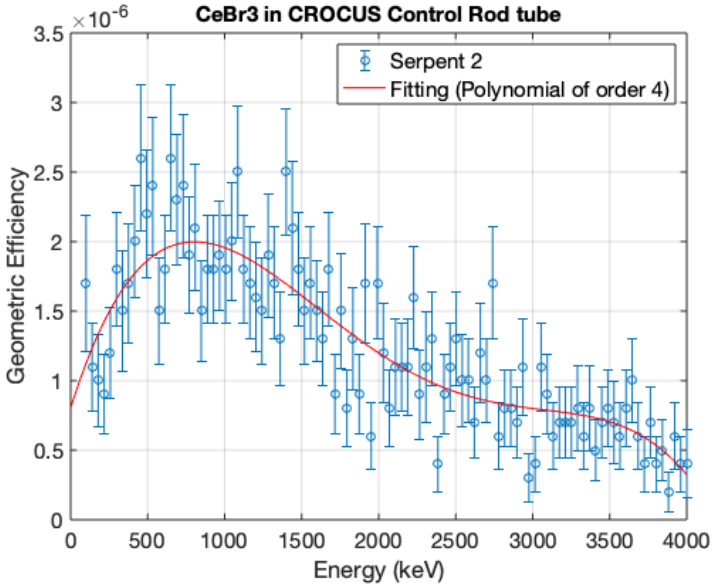

Figure 2.11: In core geometric efficiency curve for a $CeBr_3$ scintillator at 800 mm subcritical state. A water level of 800 mm corresponds to a -1.4\$ reactivity. Additional subcritical states curves are displayed in Appendix G.

In this chapter we introduced the new gamma spectroscopy system for in-core and ex-vessel measurements, respectively with $CeBr_3$ and BGO scintillators, in CROCUS. We presented a detailed geometry, characteristics and calibration to allow for explicit modelling and permit measurements for validation purposes. The next chapter will emphasis on how LEAF, as a characterized system, has been used to produce the first measurements of in-core gamma spectra and to identify and quantify delayed gamma processes in the CROCUS reactor.

Chapter 3

Gamma field characterisation in CROCUS

3.1 In-core gamma spectra in CROCUS

In-core and ex-vessel gamma spectra have been measured in the CROCUS reactor. The $CeBr_3$ scintillators were positioned in the control rod tubes, while the Bismuth Germanates were standing close but outside the vessel, both at mid-core height, as sketched Figure 3.1. CROCUS criticality is controlled by the water level and the spectra were acquired at shutdown and at five different water levels, corresponding to reactivity from -1.4$ to critical. A $ corresponds to about 750 pcm in CROCUS.

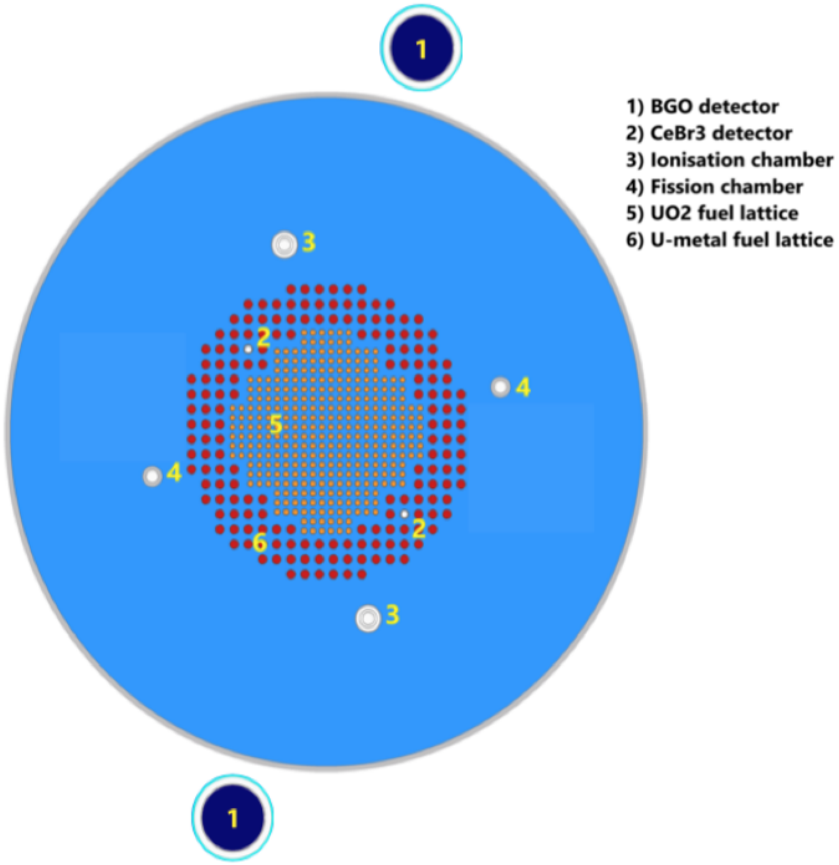

Figure 3.1: Top view of the CROCUS reactor core with LEAF system detectors locations used for noise measurements.

3.1.1 Isotope identification

The $CeBr_3$ spectra acquired at different water levels, corresponding to subcritical to critical states, are displayed in Figure 3.2. The resolution of the resolved peaks is better at shutdown and deep subcritical states where count rates do not induce dead time. All the spectra reveal a cut-off frequency around 3.3 MeV. In $CeBr_3$ crystals of $5.2 g/cm^3$, photons of 3.3 MeV have a mean free path of 3.8 cm [10], which is in agreement with the detector size (cf. Section 2.3). All the fission spectra exhibit an exponential shape. A shift in the spectrum to higher energies when approaching criticality is to be noticed, especially for the H(n,γ) peak. Thus, the peak identification has been conducted using mainly the shutdown fission spectrum. The identified isotopes can be read in Figure 3.2 and will be discussed while comparing experimental spectra to simulations in the next section.

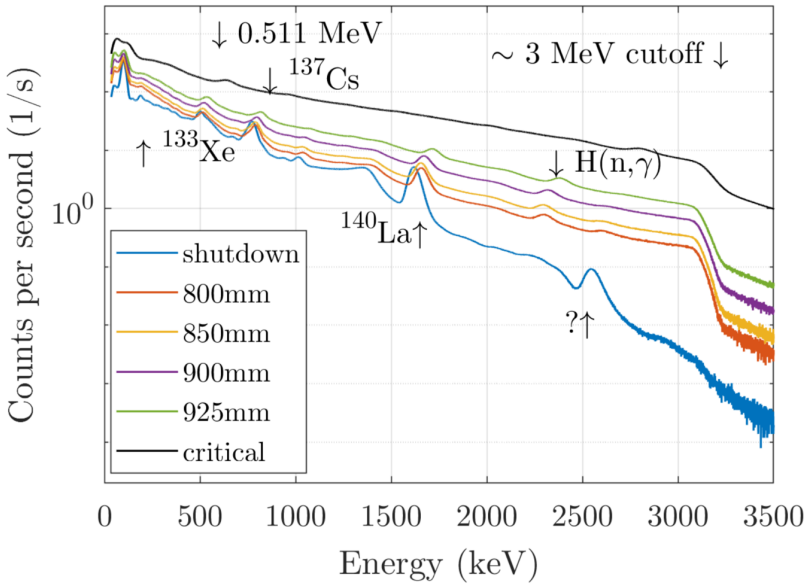

Figure 3.2: Measured in-core gamma spectra using a $CeBr_3$ detector in the control rod position for sub-critical and critical configurations. Identified isotopes are indicated directly on the curves.

The BGO spectra acquired at 500 mm water level deep subcritical state, with and without the startup neutron source, are displayed in Figure 3.3. An increase in the baseline of the spectrum measured with the neutron source due to the fission gammas can be noticed. The H(n,γ) peak is also more pronounced since more neutrons are introduced. BGO spectra acquisition aims at detecting gamma-rays at energies higher than 3 MeV, to identify fission reactions contribution to the gamma spectrum. Naturally, the spectrum base line is increased with the neutron source on. A 10 MeV cut-off energy is observed in both spectra and corresponds to the BGO crystal size (cf. Section 2.3).

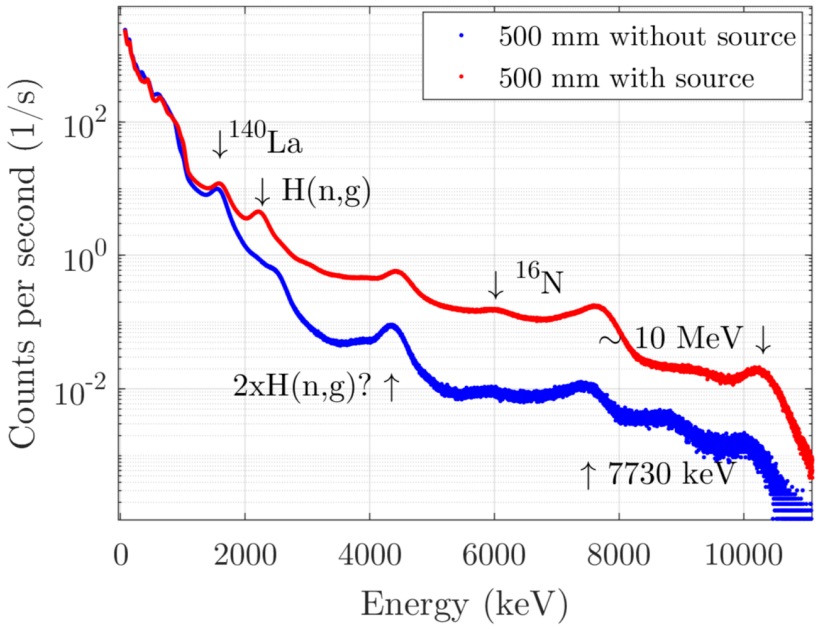

Figure 3.3: Measured gamma spectra using a BGO detector in the core vessel periphery for a water level of 500 mm -corresponding to a reactivity of -3.3$, with and without the start-up neutron source below the core. Identified peaks are indicated in the plot.

3.1.2 Application to the validation of codes

The MCNP6.2 F8 tally [11] along with the ENDF/B-7.1 was used to simulate pulse height spectra in the detectors and only include prompt processes as fission and (n,γ) reactions' photons. MCNP was preferred to Serpent since it is the established reference for critical assemblies. In Figure 3.4, we compare the MCNP pulse height tally and the thermally induced U5 prompt spectrum produced by FREYA v2.0.5 [12] to the experimental spectrum at critical. All three spectra are arbitrarily normalized to enable a qualitative comparison of the shapes. The pulse height spectrum modelled with MCNP agrees in quality with the experiments. For the analysis to go beyond visual inspection, the first of their kind in-core spectra will need refinement, especially regarding their scaling. While comparing these two spectra to the FREYA prompt fission spectrum, we can see the important contribution of the annihilation process and X-rays at energies below 0.7 MeV in CROCUS. For energies higher than 2 MeV, the MCNP pulse height tally and the experiment spectrum are lower than FREYA prompt fission spectrum which might be due to the absorption in the water reflector.

In Figure 3.5 the experimental spectrum of BGO was compared to the MCNP pulse height tally. We were able with the experiments to identify the predicted H(n,γ) both with $CeBr_3$ and BGO, the annihilation process and also fission products as Cs-137 and Xe-133 with $CeBr_3$ and La-140 and with BGO. Although BGO measurements are less conclusive regarding isotopes identification due to the large FWHM, some still unidentified peaks that were predicted by the MCNP F8 tally, as the 7.8 MeV ray, are visible in the experimental spectrum. A Serpent 2 gamma tracking history as function of energy is currently being coded so as to identify these remaining unknown isotopes.

Since resolved peaks of delayed processes not modelled in codes were identified, these experiments confirm the need for more sophisticated simulations taking missing processes into account, such as delayed emissions.

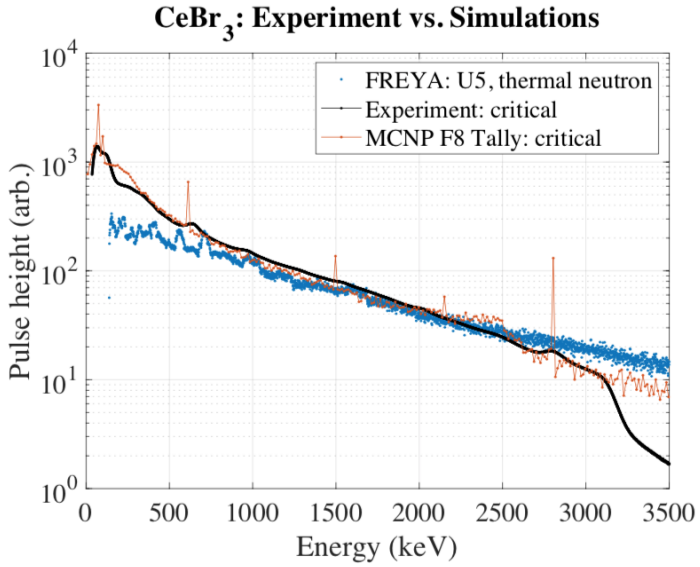

Figure 3.4: Comparison of experimental $CeBr_3$ gamma spectra to the MCNP F8 pulse height tally of the explicit model and a U-235 fission gamma spectrum obtained with FREYA. The spectra are arbitrarily normalised to their baseline between 1.5 and 2.5 MeV, to allow for visual comparison.

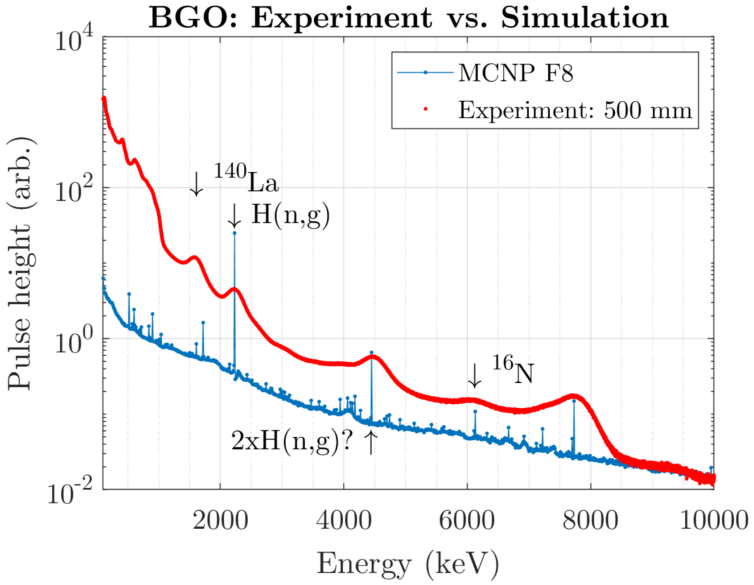

Figure 3.5: Comparison of experimental BGO gamma spectrum to the MCNP F8 pulse height tally of the explicit model. The spectra are arbitrarily normalised to their baseline above 8 MeV, to allow for comparison.

3.2 Delayed gamma determination at the CROCUS reactor by gamma-neutron measurements

The delayed processes not predicted by gamma transport codes and identified by the latest calibrated in-core gamma spectra point out the need to identify the delayed gamma contribution in reactors, and specifically in CROCUS. The LEAF system fully presented in the previous chapter, coupled to the Boron Trifluoride neutron detectors used for neutron noise measurements, provide us with the possibility of achieving a delayed gamma fraction determination in CROCUS, either integral or energy dependent.

The first studies on this subject [13] using only gamma signal decay after fast transients were not taking into account the prompt gamma contributions still ongoing after such transients, and were overestimating the delayed gamma fraction result. The latest study [14] proposing a time evolution of the delayed gamma signals strongly depends on the subjective choice made for the signals' normalisation. In this report, a new method using neutron and gamma signals, both during reactor steady operation and during fast transients, is presented. This allows the determination of the delayed gamma fraction not to be affected by signal normalisation choices.

3.2.1 Experimental setup

The gamma signal is acquired by one Cerium Bromide ($CeBr_3$) from the LEAF system, placed in the south control rod tube. The neutron signal is obtained by Boron Trifluoride neutron detectors (BF_3) placed at the peripheral positions (Figure 3.6). Ideally, neutron and gamma detectors should be placed at the same position to allow for local prompt to delayed gamma ratios determination, but since point kinetics can be assumed in CROCUS [15], the neutron flux variations are not space dependent so the neutron detector position is not important. We can thus use the classic peripheral positions for the neutron detectors and the south control rod for the $CeBr_3$. The north control rod remains in its guide tube for criticality adjustments purposes and water level is kept constant.

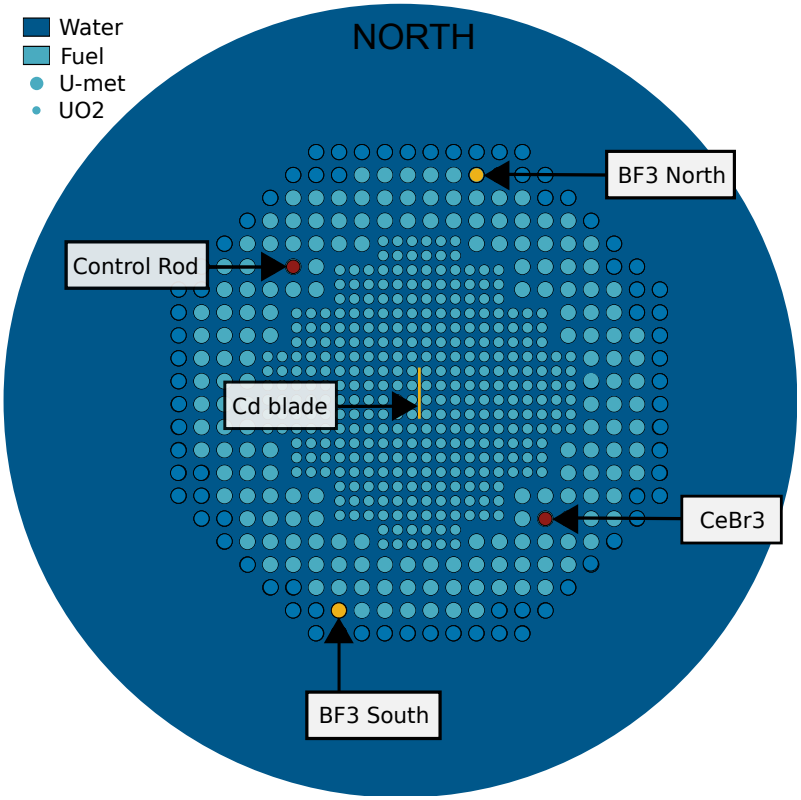

Figure 3.6: Top view of the CROCUS reactor core with detector locations used for neutron and gamma measurements.

3.2.2 Determination of delayed gamma fraction

3.2.2.1 Method

Although the delayed gammas can not be directly distinguished from the prompt in normal operation, one can use fast reactor transient during which only the prompt component of the gamma field experiences large variations. For instance, after fast reactor shutdown the gamma signal sharply drops due to the loss of its prompt fraction. Since prompt gamma rays are generated by fissions or prompt activation reactions, this prompt fraction must be proportional to the neutron signal. As a result, measuring both gamma and neutron signals during a fast reactor transient allows the delayed gamma fraction to be deduced.

The signal measured in the $CeBr_3$ scintillator, which is a combination of the delayed and prompt gamma signals, can then be expressed as function of the BF_3 neutron detector signal:

$$S_{CeBr_3} = S_{\gamma,d} + S_{\gamma,p} = S_{\gamma,d} + K \cdot S_{BF_3} \tag{3.1}$$

$$S_{\gamma,d} = S_{CeBr_3} - K \cdot S_{BF_3} \tag{3.2}$$

where:

- S_{CeBr_3}: Gamma signal obtained with the $CeBr_3$ scintillator.
- $S_{\gamma,d}$: Delayed gamma signal.
- $S_{\gamma,p}$: Prompt gamma signal.
- S_{BF_3}: Neutron signal obtained with the BF_3 neutron detector.
- K: Ratio between the neutron and gamma detectors count rates.

The delayed gamma signal is obtained by dividing Equation 3.2 by the gamma signal value during steady state reactor operation:

$$\frac{S_{\gamma,d}(t)}{S_{CeBr_3,steady}} = \frac{S_{CeBr_3}(t)}{S_{CeBr_3,steady}} - K \cdot \frac{S_{BF_3}(t)}{S_{CeBr_3,steady}} \tag{3.3}$$

This can be reformulated as

$$\frac{S_{\gamma,d}(t)}{S_{CeBr_3,steady}} = \frac{S_{CeBr_3}(t)}{S_{CeBr_3,steady}} - \frac{S_{CeBr_3,steady}}{S_{BF_3,steady}} \cdot \frac{S_{BF_3}(t)}{S_{CeBr_3,steady}} \tag{3.4}$$

by expanding the definition of K in terms of signals ratio instead of count rates ratio.

Finally, the normalised delayed gamma signal can be written:

$$S_{\gamma,d,norm}(t) = S_{CeBr_3,norm}(t) - S_{BF_3,norm}(t) \tag{3.5}$$

where $S_{norm} = S(t)/S_{steady}$.

One must pay attention to the validity domain of this formula. In this method, both gamma and neutron signals are normalised at steady state, before any transient occurs. This means the delayed gamma signal defined in Equation 3.5 is only valid after the transient considered. These considerations will be explored in detail in the following subsection.

3.2.2.2 Experimental procedure

In order to apply the methodology exposed in the previous subsection, a steady state reactor operation at criticality should be followed by a fast negative reactivity insertion transient.

Fast reactor shutdown Transients commonly used in previous experiments of this kind ([14], [13]) were fast reactor shutdown (SCRAM). Contrary to the JSI TRIGA reactor [14] which can reach a power of 10 kW, CROCUS is mostly operated at power lower than 1 W. Therefore, gammas from long-lived isotopes should contribute a lot more to the delayed gamma fraction in the zero power reactor CROCUS than in the JSI TRIGA reactor. CROCUS reactivity is also monitored by the water level and SCRAM induces the draining of the vessel. The resulting water movement causes oscillations in the neutron and gamma signals, which can be seen on Figure 3.7.

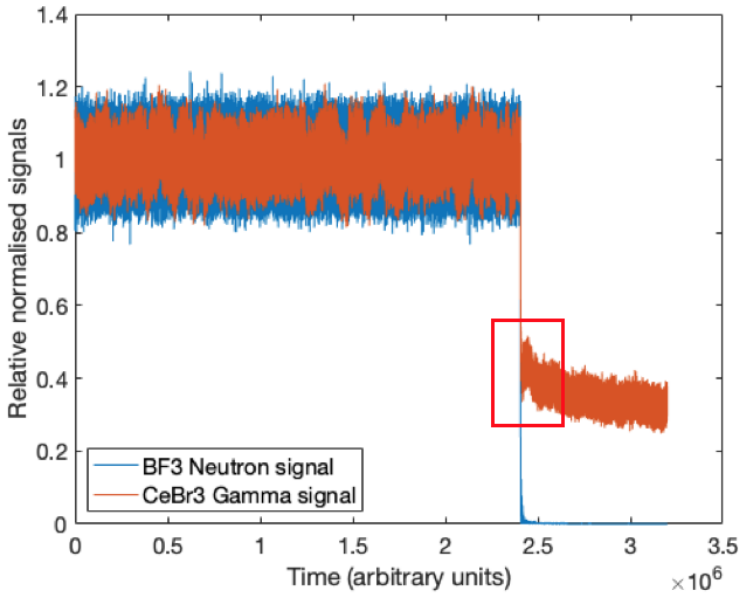

Figure 3.7: Neutron and gamma signals from the SCRAM experiments. Signals are normalised at their steady state average values before SCRAM. The water oscillation can be seen in the red square.

Figure 3.8: Screenshot from the control room camera. The Cadmium blade is right in the middle of the two safety blades.

Cadmium blade drop To avoid the water oscillations aforementionned, a cadmium blade drop was preferred to perform a quick reactivity insertion without changing the water level. This blade can be seen on Figure 3.8.

Usually, the water level corresponding to criticality with the LEAF setup installed is around 962 mm. For this experiment, we chose to operate at a water level of 975 mm and 30 mW power. Even if the reactivity drop is no more caused by a draining of the vessel, the cadmium blade insertion might still cause some small water oscillations. To minimize this potential effect, we chose to operate at a higher water level than the usual 962 mm used for critical noise measurements. Since the south control rod tube contains the $CeBr_3$, only the north control rod remains to insert negative reactivity. For criticality to be reached, its position has to be set to 532 mm. The power level was chosen to satisfy both $CeBr_3$ and BF_3 count rates which are order of magnitudes different. The reactor should be operated at the higher power possible for the BF_3 to count enough gammas during the decay after the cadmium blade insertion, but without triggering too much the $CeBr_3$ dead time, especially paralysable. At a power of 30 mW with respectively 2.8 kHz and 300 kHz for BF_3 and $CeBr_3$, both conditions were respected.

The experiment timeline is the following, as represented in Figure 3.9:

- $t = 0$: start of gamma and neutron signal acquisition
- $t = t_0$: neutron source introduction
- $t = t_1$: "manuel" state on (safety blades pulled out and water rising from 500 to 800 mm)
- $t = t_2$: water level set to 975 mm and control rod pulled out to increase power up to 30 mW in supercritical state
- $t = t_3$: control rod inserted down to 532 mm to reach criticality

- $t = t_4$: power stabilized at 30 mW
- $t = t_5$: Cadmium blade drop.

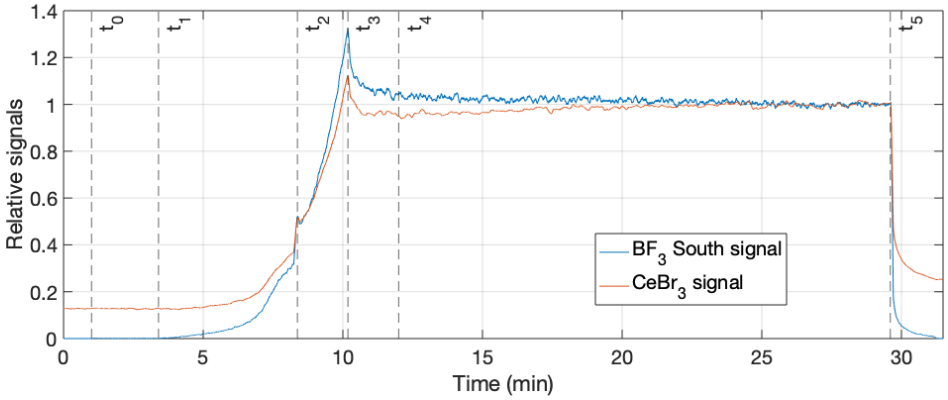

Figure 3.9: BF_3 neutron signal and $CeBr_3$ gamma signal, both normalised to their value at $t = t_5$. The gamma build-up due to delayed contributions can be seen between t_4 and t_5. The horizontal dotted line represents the delayed gamma contribution from long-lived isotopes.

3.2.3 Results

A key point in the determination of the delayed gamma fraction is the choice of the neutron and gamma signals normalisation point. For illustrative purposes we will first assume that it should be done at $t = t_{5-}$, i.e. just before the Cadmium blade drop. The delayed gamma signals, as introduced Equation 3.5, is then displayed in Figure 3.10.

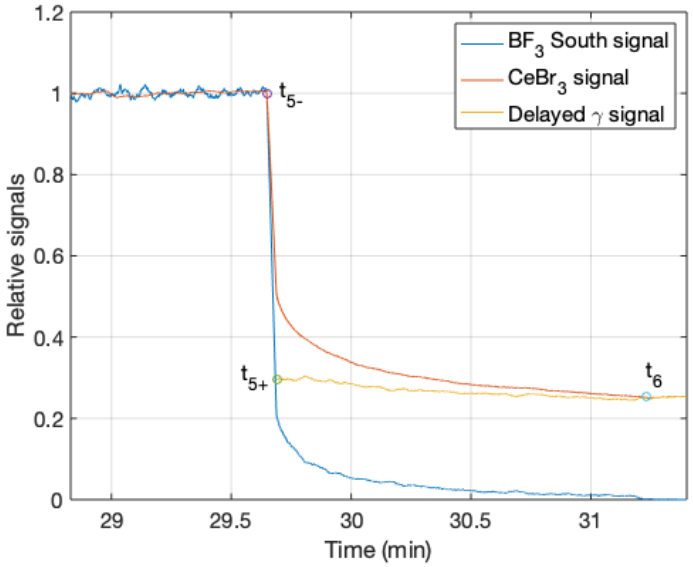

Figure 3.10: Neutron, gamma and delayed gamma signals decays.

Right after the Cadmium blade insertion, the delayed gamma signal reaches its delayed gamma fraction value:

$$F_{\gamma,d} = S_{\gamma,d,norm}(t_{5+}) \tag{3.6}$$

In order to precisely determine this $F_{\gamma,d}$ value, the delayed gamma signal decay was fitted between t_{5+} and t_6 with a two term exponential, to take into account both delayed gammas from fission products and long-lived activation products contributions. The fit was only performed before t_6 since after this time the BF_3 count rate was too low to provide a reliable neutron decay.

This method was then repeated for 100 different neutron and gamma signal normalisation points between t_4 and t_{5-}. The results are shown Figure 3.11.

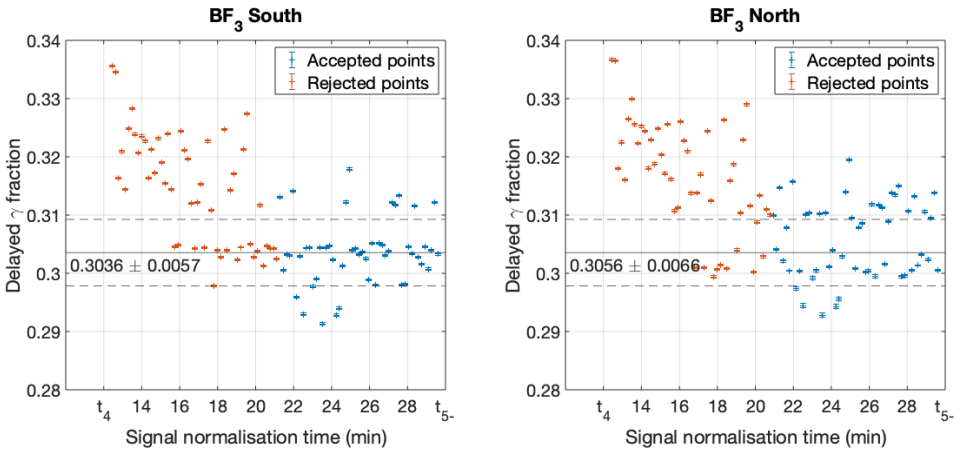

Figure 3.11: Delayed gamma fraction $F_{\gamma,d}$ as a function of the signal normalisation time. 100 points scaled between t_4 and t_{5-}, for both BF3 positions. The averaged values of the "accepted points" and its standard deviation can be read.

The plots from Figure 3.11 should be read closely with Figure 3.9 for a better understanding. Each delayed gamma fraction from Figure 3.11 corresponds to a different normalisation of Figure 3.9 neutron and gamma signals. In Figure 3.9, both signals are normalised at t_{5-}, but to produce the results from Figure 3.11, 100 normalisation points were performed between t_4 and t_{5-}. Then, for each of these normalisations, which are leading to plots similar to Figure 3.9, a two term exponential fit between t_{5+} and t_6 is done and the delayed gamma fraction is obtained as described Equation 3.6.

The delayed gamma fraction distribution, from plots Figure 3.11, both present a similar trend. First a decrease from normalisation time t_4 to $t = 20$ min and then a stabilisation around a mean value displayed on each plot. By keeping in mind Figure 3.9, we can infer that delayed gammas take about 8 minutes from the power stabilisation that occurred at t_4 to build up. Therefore, the signal normalisation should not be done before $t = 20$ min. "Accepted points" refer to the values after $t = 20$ min and were the only considered in the

establishment of the means and standard deviations. Despite this clear cut off at $t = 20$ min, several points were already closely concentrated around the average delayed gamma fraction value.

The delayed gamma fractions around the south and north control rods, inferred from the mean and standard deviations of the data in Figure 3.11, can be read Table 3.1.

Table 3.1: Delayed gamma fraction in CROCUS South control rod.

BF3 position	$F_{\gamma,d}$
South	0.3036 ± 0.0057
North	0.3056 ± 0.0066

Delayed gamma fractions for both BF_3 neutron detector positions are compatible within their standard deviations, which confirms the validity of the method.

Discussion In experiments conducted at the JSI TRIGA reactor [14], a quick reactor startup is followed by a fast shutdown, after steady state is reached both in the gamma and neutron signals. Both signals are normalised as soon as steady ractor power is reached. Then, the gamma signal increases, as delayed gammas start to build up, and it saturates to a steady state value. The delayed gamma fraction is assimilated to the steady state value reached by the normalised gamma signal after delayed gammas have built up. One can argue that the gamma signal will never reach a constant value since gammas from activation products will always add up to the signal. This slight increase is due to long-lived activation products which contribution can be neglected at the JSI TRIGA reactor when operated at 50 W to 10 kW. However, this is not the case in CROCUS since at low power operation the gamma background contribution to the whole gamma field can not be neglected. Thus, a methodology where the delayed gamma fraction determination is performed after the transient occurred was there preferred. Moreover, we performed a full investigation on the signals' normalisation point for the delayed gamma fraction result not to lay on a visual estimation.
Although previous delayed gamma fraction evaluation performed after fast transients, as [13], was leading to an overestimation of the delayed gamma fraction, the influence of the neutron signal has been here taken into account and removed from the delayed gamma signal after the transient occurred. The delayed gamma fraction obtained in CROCUS is very similar to the one obtained at the JSI TRIGA reactor core centre, delayed gamma contribution due to long-lived isotopes being more pronounced in low power reactor CROCUS than in JSI TRIGA though. To have a gamma background lower than 1% of the full gamma signal, CROCUS should be operated at more than 381±9 mW, but the $CeBr_3$ dead time issues arise at such power.

Outlook These results coupled to the first in core gamma spectra provided by the LEAF system opens the possibility of delayed gamma fraction determination as function of energy

in CROCUS. Cerium Bromides scintillators provide us with well resolved in-core spectra under 3 MeV while Bismuth Germanates allow acquisition up to 10 MeV, so that the LEAF system allows for a wide identification of gamma emitters present in CROCUS. This knowledge added to nuclear data enables an estimation of the relative contribution of each isotope to the whole spectrum. This can help code validation by stating if the contribution of a specific isotope is under or overestimated by the simulation. It can also allow to draw the time dependence of the building up of each isotope identified.

Chapter 4

Zero power noise measurements in CROCUS with the new LEAF system

Neutron noise is a non-invasive method to determine kinetics of a reactor through its prompt decay constant, effective delayed neutron fraction and mean generation time. Instead of performing dynamic experiments, as control rod drop or ejection tests, kinetic parameters could be inferred from measurements at steady-state and contribute to databases for code validation. Besides the typical neutron noise measurements, gamma-rays potential has been of interest [16], [17], [18] as the higher mean free path would in principle permit ex-core detector positioning. This chapter will introduce the nuclear reactor kinetics theoretical basis needed for reactor noise analysis and present the first gamma noise measurements performed with the LEAF system in the CROCUS reactor.

4.1 Point kinetics and reactor noise

4.1.1 Boltzmann transport equation to point kinetics

The Boltzmann equation, which was firstly used to describe the kinetic of gases, received neutron transport developments with the advent of the first nuclear reactors. It was indeed motivated by the need to predict the generated power to adapt accordingly the cooling system. Since the reactor power is strictly proportional to the neutron flux, the Boltzmann neutron transport equation describes the evolution in time of a neutron population as a function of energy direction and position [19]. To study the kinetic behaviour of a neutronic system, this equation is almost never deterministically solved with its full space, energy, angle and time dependence, but rather approximated by diffusion theory when possible, or treated by stochastic methods as Monte Carlo methods. However, if the independence of the neutron density with respect to space and energy can be assumed, point kinetics equations (Equations 4.1 and 4.2) can be obtained from the general neutron transport equation. How point kinetic equations can be derived from the Boltzmann neutron transport equation is thoroughly presented in Appendix H.

$$\frac{dA}{dt} = \frac{\rho - \tilde{\beta}}{\Lambda} A + \sum_i \lambda_i C_i + S \tag{4.1}$$

$$\frac{dC_i}{dt} = \frac{\tilde{\beta}_i}{\Lambda} A - \lambda_i C_i \tag{4.2}$$

with $C_i = \frac{(N_0^\dagger, \epsilon_i)}{\Lambda F}$.

where:

- A: time dependant amplitude of the neutron density.
- C_i: time dependant quantity of precursor i per unit volume.
- $F = (N_0^\dagger, \hat{\boldsymbol{M}}\varphi)$: total importance associated to the shape of the flux.
- $\rho = \frac{(N_0^\dagger, \boldsymbol{\delta}\hat{\boldsymbol{H}}\varphi)}{F}$: reactivity.
- $\tilde{\beta} = \frac{(N_0^\dagger, \sum_{\boldsymbol{i}} \hat{\boldsymbol{M}}_{\boldsymbol{i}}\varphi)}{F}$: effective delayed neutron fraction.
- $\Lambda = \frac{(N_0^\dagger, \varphi)}{(N_0^\dagger, \hat{\boldsymbol{M}}\varphi)}$: prompt generation time.

These parameters are sufficient to describe a reactor's transients and therefore constitutes the reactor characteristics. Determining these kinetic parameters is the preliminary work to any solving of the point kinetic equations.
A reactor in which the point kinetics equations are valid is a point reactor. In such a reactor the neutron density amplitude evolves without changing its shape. CROCUS can be considered as a point reactor [15].

Equations 4.1 and 4.2 form a system of first order differential equations. Its solution can thus be written as a sum of exponentials:

$$A(t) = \sum_j A_{0j} e^{\alpha_j t} \tag{4.3}$$

where the A_{0j} coefficients depend on initial conditions. The first exponent is the prompt neutron decay constant α_p explicited in Equation 4.4 , while α_2 to α_7 are related to delayed neutrons contributions. After introducing A_0 neutrons into our reactor, the neutron population will exponentially decay with an α_p constant.

$$\alpha_p = \frac{\rho - \tilde{\beta}}{\Lambda} \tag{4.4}$$

4.1.2 Reactor noise

It refers to the temporal fluctuation of the power around its steady-state deterministic constant value [1]. It can be induced by thermal noise, flicker noise, interferences, or by spontaneous processes as radioactive decays emitting particles with a constant mean rate. In this last case, the resulting detector signal follows a Poisson distribution, while in presence of correlated sources, deviations from the Poisson distribution can be observed.

A distinction is to be made between **zero power noise** and **power reactor noise**. In systems where thermo-hydraulic and mechanical noise effects can be neglected, the observed power fluctuations are referred to as zero power noise or branching noise. This type of noise only depends on fission chains probabilistic processes, as the amount of neutrons emitted per fission ν, the time between nuclear interactions τ, or the fission and absorption cross sections. Zero power noise analysis stands in the measurement of temporal correlations happening while detecting neutrons from the same fission chains successively. Power reactor or external noise arises from mechanical vibrations, induced by coolant flow, coolant boiling or local temperature variations, and is causing local macroscopic cross sections to fluctuate. These vibrations can also be actively induced by rod oscillation as performed in the COLIBRI experiment [20]. This chapter will lay emphasis on zero power noise.

4.2 Zero power reactor noise analysis methods

This section is adapted from O.Pakari's thesis [1] and should be referred to for further details.

The most notable methods for zero power noise analysis are the auto correlation or Rossi-α, the variance over mean or Feynman-α and the power spectral density or PSD method. All three are based on the measurement of subsequent pulses from a neutron detector close to the reactor in order to inspect the statistics of the time between pulses in time or frequency domain.

Rossi-α method It relies on measuring the time difference between subsequent pulses of a detector, which relates to the auto correlation of the neutron population. Assuming a detection of a neutron at a time t_0, a second detection t can originate either from unrelated fission chains or from the same fission chain in a prompt process. Neglecting neutrons in the fission chain, the total detection probability at time t within a detection time dt can thus be written:

$$p(t)dt = F\epsilon(A + Be^{-\alpha_p t})dt \tag{4.5}$$

with α_p describing the exponential decay of probability to detect a neutron from the same

prompt chain. The constant A describes the uncorrelated detection of two neutrons and is found to be the count rate of the detector:

$$A = F\epsilon \tag{4.6}$$

where F is the fission rate of the system and ϵ the detector efficiency in counts per fission in the reactor. B describes the detection of neutrons coming from the same fission chain, called correlated neutrons:

$$B = \frac{\epsilon D_\nu}{2\alpha_p \Lambda^2}. \tag{4.7}$$

D_ν is the Diven factor which relates to the prompt neutron yield per fission. As a result, the prompt decay constant α_p can be assessed from the shape of the auto correlation curve.

A second detector can be used and the cross correlation between the two is used instead.

Feynman-α method It is based on the measurement of variance and mean value of counted neutrons of a variable time bin t. As described in section 4.2.1 the reactor power and therefore the neutron flux will fluctuate around a mean value. These fluctuations originate from random or correlated events in fission chains. Therefore, counts in a detector Z during a time gate t depend on a constant contribution given by the mean neutron population and a noise contribution characterized by a variance which is correlated to reactor nuclear characteristics. The Feynman-α method relates the variance to mean ratio of the detector signal Z to the branching noise:

$$\frac{\bar{Z^2} - (\bar{Z})^2}{\bar{Z}} = \frac{Var(Z)}{Mean(Z)} = 1 + \frac{\epsilon D_\nu}{(\rho - \beta_{eff})^2}\left(1 - \frac{1 - e^{-\alpha_p t}}{\alpha_p t}\right) \tag{4.8}$$

Contrary to phenomenon with constant mean rate described by Poisson distribution, where the variance to mean ratio is equal to one, in a nuclear reactor the variance is higher due to the multiplication process. The variance to mean ratio depends on the time gate t. For very short t $<$ 1ms, it seems to be one, while for longer gates, the variance increases. The prompt decay constant α_p can be deduced from the shape of this time dependence.

As for the Rossi-α method, a second detector can be used and the covariance to mean ratio is performed instead:

$$\frac{\bar{Z_1 Z_2} - \bar{Z_1}\bar{Z_2}}{\bar{Z_1 Z_2}} = \frac{Cov(Z_{1,2})}{\sqrt{Z1,2}} = \frac{\epsilon^2 F_0 D_\nu}{(\rho - \beta_{eff})^2}\left(1 - \frac{1 - e^{-\alpha_p t}}{\alpha_p t}\right) \tag{4.9}$$

Power Spectral Density method It transfers the Rossi-α auto correlation to the frequency domain by taking its Fourier transform:

$$G_{xy}(w) = \int_{\infty}^{-\infty} dt e^{-iwt} p(t) = \epsilon F + \frac{\epsilon^2 F D_\nu}{\beta_{eff}^2} \frac{1}{1 + w^2/{\alpha_p}^2} \tag{4.10}$$

This results in a Lorentzian bell curve with a cut-off frequency at α_p. The Fourier transform of the cross-correlation function is:

$$G_{xy}(w) = \int_{\infty}^{-\infty} dt e^{-iwt} p_{1,2}(t) = \frac{\epsilon^2 F D_\nu}{\beta_{eff}^2} \frac{1}{1 + w^2/{\alpha_p}^2} \tag{4.11}$$

These analysis methods presented here for neutron correlations can also be applied to gamma and neutron-gamma correlation measurements [21].

4.3 Experimental realisation of zero power noise measurements

This section aims at presenting how from the detectors amplified signals are produced and fitted Rossi, Feynman or Cohn-α curves. The three methodologies are explained here after and summed up Figure 4.1.

4.3.1 From time dependant counting to noise analysis

Rossi-α The measurement time stamps between each detector counts are registered and the number of occurrences for each time stamp is sorted out with respect to time stamp length. This results in a Rossi-α curve. In practice, the auto correlation function of the signal acquired with a dwell time of 500 μs is calculated.

Feynman-α For a defined gate length, also called dwell-time, detector counts are registered. Then, the number of counts per segments, for each gate length, are sorted out in histograms. The variance to mean ratio for each histogram is calculated in order to produce a Feynman-α curve. In practice, a gate length of 500 μs is taken to produce the histogram with the smallest gate length and then sum of segments are taken to get larger gate length histograms [1].

Power Spectral Density PSD curves -sometimes also called Cohn-α curves- can be obtained from two different ways. Either by taking the Fourier transform of the Rossi distribution, or by taking a specific histogram from the Feynman approach and applying the Bartlett PSD estimation method. The gate length of the chosen histogram, which corresponds to the sampling frequency of the signal, should exceed the double of the frequency we want to observe with respect to the Nyquist-Shannon theorem. Taking the Fourier transform of the auto correlation function to produce PSD curves is in practise never performed. Instead, the Fourier transform of the 500 μs gate length histogram, corresponding to a 2000 Hz sampling rate, is taken and multiplied by its complex conjugate. The resulting PSD curve is called periodogram. The Bartlett method consists in cutting the full signal into segments, calculating the PSD curve for each and averaging it. It is thus reducing the variance of the periodogram, but reducing its resolution. The segment length should be long enough for the branching phenomenon to be contained in, but order of magnitudes shorter than the full signal to get a smooth averaging. For noise experiments a window size that yields a spectral resolution under 0.5 Hz is needed [1].

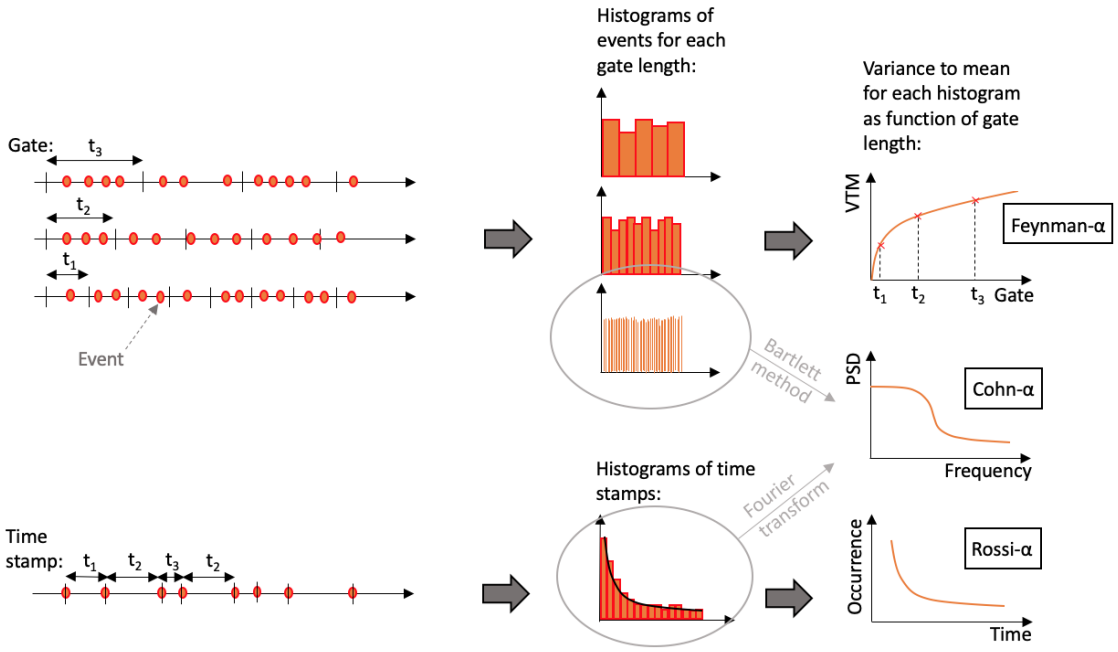

Figure 4.1: Schematic of the experimental realisation of noise analysis methods. Adapted from [1].

4.3.2 Noise curve fitting

In order to obtain kinetic parameters as the prompt decay constant α_p, these curves need to be fitted. The functions used to this purpose are presented in section 4.3 and are based on the point kinetics equations. The goodness of the fitting result relies on the residuals function of the fit. If the residual distribution is normally distributed around the fit, the model considered is accurate. Residuals can be defined either as the vertical distance be-

tween the date point and the fitting curve or by the square of it in order to discriminate more outliers. Usually, methods as the Maximum Likelihood Estimation (MLE) are used in order to find the best parameters for a model to best fit the data. However, assuming Point Kinetics to apply to CROCUS, we can be confident in the trueness of our models and directly use the Ordinary Least Squares estimator (OLS) for residuals. According to the Gauss-Markov theorem [22], the OLS stands as the Best Linear Unbiased Estimator (BLUE) for linear regression models. Although we are considering strongly non-linear models, we will take the OLS estimator as a first guess.

We are thus able to obtain the best fit parameters for our models, as the α_p. The standard deviation of this parameter is obtained as follows. According to [23], the Hessian matrix of the residual function is equal to the inverse of the covariance matrix:

$$COV = H^{-1} \cdot MSE \tag{4.12}$$

where COV is the covariance matrix, H is the Hessian matrix of the residual function containing all the residuals derivatives. The mean squared error (MSE) of the residuals is used to weigh the Hessian matrix. The high order terms of the Hessian matrix are very difficult to estimate so by Taylor expanding it to the first order we get:

$$COV = (J^T J + O^2) \cdot MSE \tag{4.13}$$

with J being the Jacobian of the residuals function. As a first estimate, second order terms are considered to be negligible since second and higher order gradients of the residuals function would mean that the residuals' distribution is not normal. The results are thus presented assuming a first order approximation on the residuals. This assumption should be verified with Monte Carlo methods as Bootstrapping for the uncertainties' estimation [24].

4.3.3 Parameters influencing the curve fitting

Any data set can be fitted by a model. However, not all the fits will result in an accurate estimation of our model's variables.

Rossi's distributions and PSD curves are carrying the same physical information but in different domains, respectively time and frequency. Therefore, the fitting of the Rossi exponential and of the Cohn Lorentzian should provide the same α_p. However, according to the investigations developed in Appendix I, the fitting of PSD curves should be preferred to the fitting of Rossi distributions regarding the obtention of the prompt decay constant.

The cut-off frequency estimation of the PSD curve through the fitting of the Lorentzian strongly depends on the PSD amplitude plateau. Essentially, the higher the amplitude of this plateau, the easier a cut-off frequency can be distinguished and the better the fit result [1]. However, several parameters are influencing the PSD amplitude: the count rate, the energy of the incident gammas, the detector efficiency and the white noise amplitude around

the averaged PSD shape. Although in neutron noise the three first parameters all have the same effect on the PSD amplitude, in gamma noise they have independent behaviours. This is discussed in Appendix J while trying to determine the optimum threshold for the gamma correlation measurements with the Cerium Bromides detectors. To be succinct, increasing the threshold, which means considering higher energy gammas for correlations, is increasing the CPSD amplitude, but also drastically reduce the count rate and therefore the statistics. A trade off has to be found.

Regarding Feynman-α curves, the information on the prompt decay constant is not localised but contained in the whole flexion of the curve. As long as the Feynman variance to mean (VTM) curve is neither flat nor linear, it seems to be fittable with a multi exponent model. Multi exponent fitting also provides better results for PSD. While Feynman fits are very sensible to starting points, PSD fits are really robust.

4.4 Neutron and gamma correlation measurements

A first campaign of neutron correlations measurements with He-3 detectors at subcritical states was conducted in 2018 and the results are standing as the reference data set. In late 2019, gamma correlation experiments have been conducted thanks to the LEAF setup with the following targets: Can we see gamma noise in CROCUS? If we are able to determine kinetics parameters as the prompt decay constant α_p, is it accurate and reliable compared to the neutron noise reference? To what extent, regarding the reactivity and distance variables, do we see noise? This section aims at answering these points.

4.4.1 Neutron noise reference measurements

A series of neutron correlations measurements with He-3 detectors have been performed in CROCUS in 2019. These experiments covered five subcritical states and five detector positions around the fuel with two hours measurements each [25]. The configurations were arbitrary chosen to cover reactivity worths from -1.4$ to critical and several in-vessel positions up to 20.15 cm from the fuel. The α values obtained for the five subcritical states at the closest distance to the fuel (4.65 cm), and an additional critical measurement, will be considered as the "Neutron Noise Reference" in the following sections. Prompt decay constants simulated with Serpent 2 are also displayed in table 4.1 to allow for comparison.

4.4.2 Experimental setup for gamma noise measurements

The classic LEAF setup positioning used for in-core and ex-vessel spectroscopy, with two additional Boron Trifluoride (BF_3) neutron detectors in peripheral positions is used. The handling of the high voltage supply and the output signal of these six detectors is described in Appendix K. While $CeBr_3$ scintillators will always stay in the control rod tubes, the Bismuth Germanates will be gradually removed from the vessel, according to the mapping presented in Figure 4.2, so as to investigate how gamma noise evolves with distance compared to neutron noise limited range. From locations 2 to 5, the BGO detectors are

symmetrically removed from the core. Then, in location 6, the north BGO is placed into the cavity hole while the south one is moved to the cavity north corner. In location 7, the north BGO is moved deeper into the hole and the south one is kept at the north corner of the cavity but placed behind a lead shield. From positions 8 to 11, both BGO are placed side by side, outside the cavity, in direct line with the core. In location 9, the threshold was set to 0.5 V instead of 0.1 V as in all the other experiments to confirm the hyphotesis discussed in Appendix J.

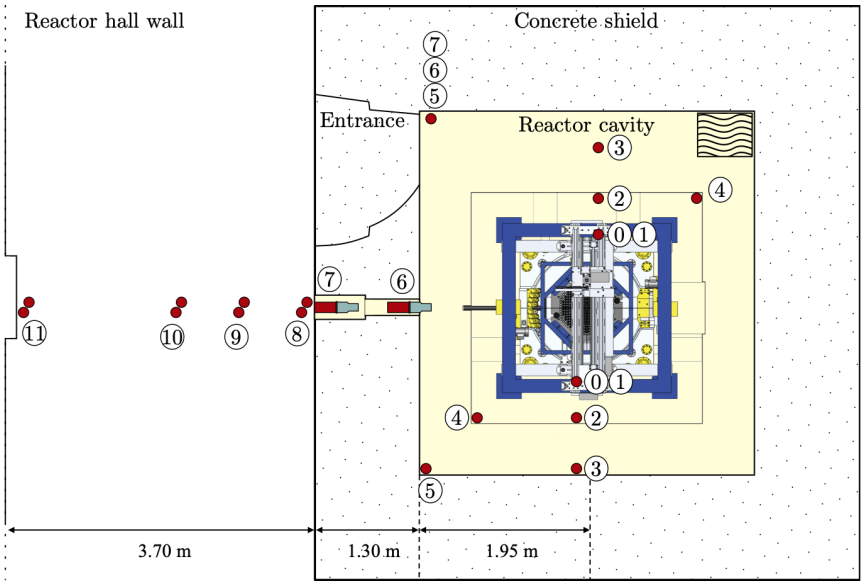

Figure 4.2: Top view of the CROCUS hall with all BGO positions used for distance noise measurements. Adapted from [1].

4.4.3 Cerium Bromide measurements

$CeBr_3$ detectors, which can fit inside the control rod tubes, constitute the in-core measurements tools of the LEAF system. Already providing well-resolved in-core spectra, they have also been used to reproduce the reference neutron noise measurements with He-3 detectors. Thanks to the BF_3 detectors in peripheral positions, we were also able to perform another kind of neutron correlation measurements, for comparison with the existing He-3 data. It also allows for neutron-gamma correlations. All the results are presented in Appendix L.

Gamma noise best results in term of alpha reliability are provided by Cohn-α CPSD curves, and Feynman-α CTM curves both fitted with multiple exponent functions (cf. Section 4.4.3). The results of Figure 4.3 show that both methods are providing prompt decay constant α very similar to the neutron noise reference measurements but uncertainties are lower with CPSD. Numerical values are presented in Table 4.1.

Table 4.1: Subcritical and critical alphas obtained with $CeBr_3$ correlations measurements compared to the He-3 reference measurements and to Serpent 2 simulations.

Water level (mm)	Reactivity ($)	CTM α (1/s)	CPSD α (1/s)	Reference α (1/s)	Serpent 2 α (1/s)
800	-1.4	398.1 ± 17.3	377.21 ± 0.59	377.52 ± 2.35	389.91
850	-0.9	309.89 ± 3.32	293.54 ± 0.28	296.84 ± 1.42	306.39
900	-0.5	230.83 ± 2.57	226.33 ± 0.24	231.1052 ± 0.93	234.20
925	-0.3	198.58 ± 1.56	195.12 ± 0.10	199.92 ± 0.71	202.49
950	-0.1	165.78 ± 0.53	161.19 ± 0.08	176.02 ± 0.85	172.34
962.8	0	154.42 ± 1.52	147.56 ± 0.06	154.2 ± 2.1	158.60

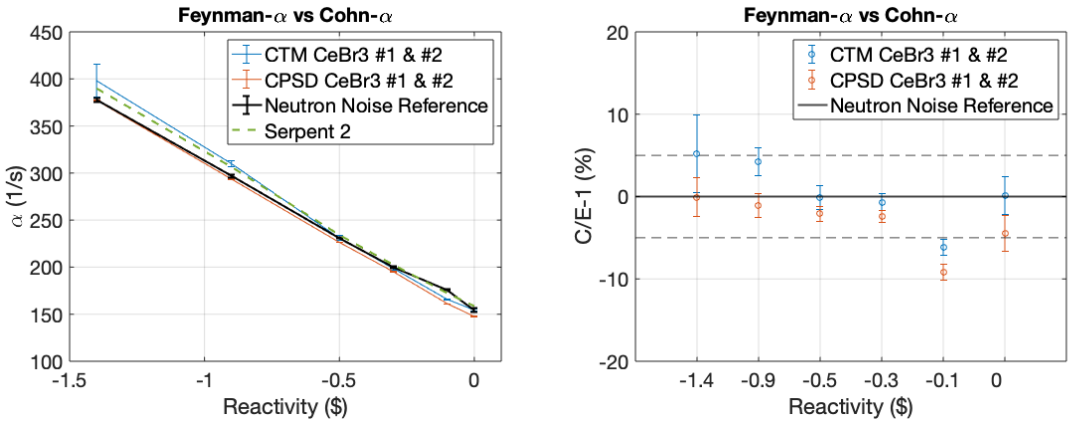

(a) **(b)**

Figure 4.3: (a) Prompt gamma decay constants, obtained with CTM and CPSD methods, both as function of reactivity. (b) Comparison of CTM and CPSD prompt gamma decay constant to the neutron noise reference

In Figure 4.4, the influence of the correlation type on the CPSD fitting, as function of the measurement time, is plotted. Both the prompt decay constant and its relative standard deviation evolutions with time are shown. BF_3 neutron correlations, $CeBr_3$ gamma correlations and mixed neutron-gamma correlations are compared to the He-3 neutron reference. It emerges that gamma correlations with $CeBr_3$ need as short measurements as neutron correlations with He-3 to converge on reliable prompt decay constants. Gamma correlations are also providing us with the smallest uncertainties among all types of correlations (cf. right y-axis of Figure 4.4).

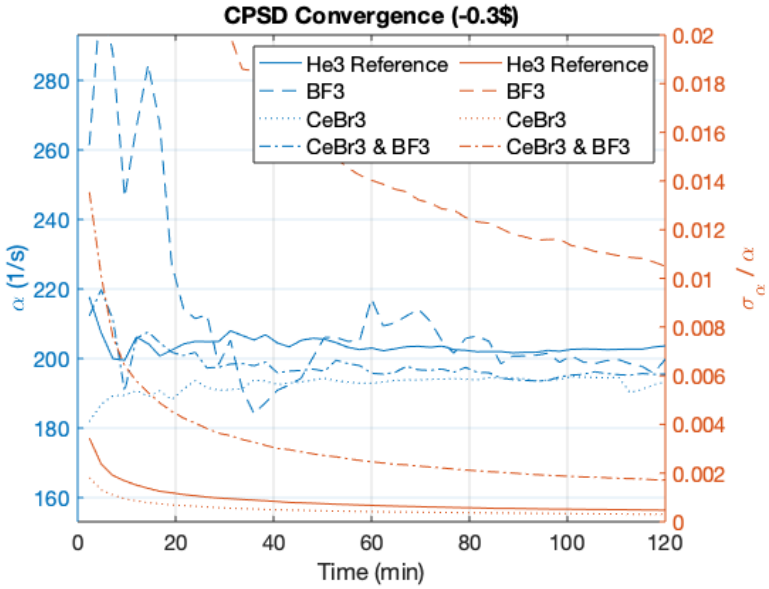

Figure 4.4: Prompt gamma decay constant and its relative uncertainty as function of the measurement length, for $CeBr_3$ gamma correlations, BF_3 neutron correlations, neutron-gamma correlations with these very same detectors, and He-3 reference neutron correlations. Same plots for other reactivity levels are shown in Appendix L.

4.4.4 Bismuth Germanate distance measurements

BGO scintillators, allowing for ex-vessel gamma spectra acquisitions account for the high efficiency detection devices of the LEAF system. While He-3 neutron correlation measurements were performed in vessel at 20.15 cm maximum from the core with poor results [1], gamma correlation measurements were successful at the reactor hall wall , i.e. outside the reactor cavity (Figure 4.2), at 6.95 cm from the core centre.

While $CeBr_3$ measurements aim at reproducing the neutron noise reference data with high fidelity regarding the prompt decay constants, these BGO measurements aspire to find the gamma noise "limit" distance for CROCUS. To that end, this study stresses on the Feynman and Cohn-α curves shape evolution with detector distance to the fuel, more than on their fitting for prompt decay constant determination purposes. The different measurements done are listed in Table 4.2.

Table 4.2: Measurement time in hours for each BGO location and reactivity investigated.

Position (id)	800 mm ≈ -1.4\$	900 mm ≈ -0.5\$	950 mm ≈ -0.1\$	20 mW Critical
1	-	0.5	-	2.0
2	-	0.5	-	-
3	0.5	0.5	-	-
4	0.5	0.5	-	-
5	0.5	0.5	-	-
6	0.5	0.5	-	-
7	0.5	0.5	-	-
8	-	0.5	-	-
9	-	0.5	0.5	-
10	-	0.5	0.5	-
11	-	-	-	2.0

The CTM and CPSD curves for several BGO distance to the core are shown in Figures 4.5a and 4.5b. The detectors' locations are reminded in Figure 4.5c. While CTM curves amplitude are decreasing with distance, an opposit phenomenon is observable with CPSDs. From locations 2 to 6 the amplitude is increasing. In Figures 4.5d and 4.5e), count rates and CPSD amplitudes are plotted for positions 2 to 10. While count rates are decreasing with distance as expected -variations due to shielding left aside-, the CPSD amplitude is globally increasing. It appears that removing detectors from the core has the same effect on the CPSD amplitude as increasing the threshold (cf. Appendix J). Increasing the distance results in filtering out the low energy gammas and, therefore, correlated events seem to originate only in high energy gammas.

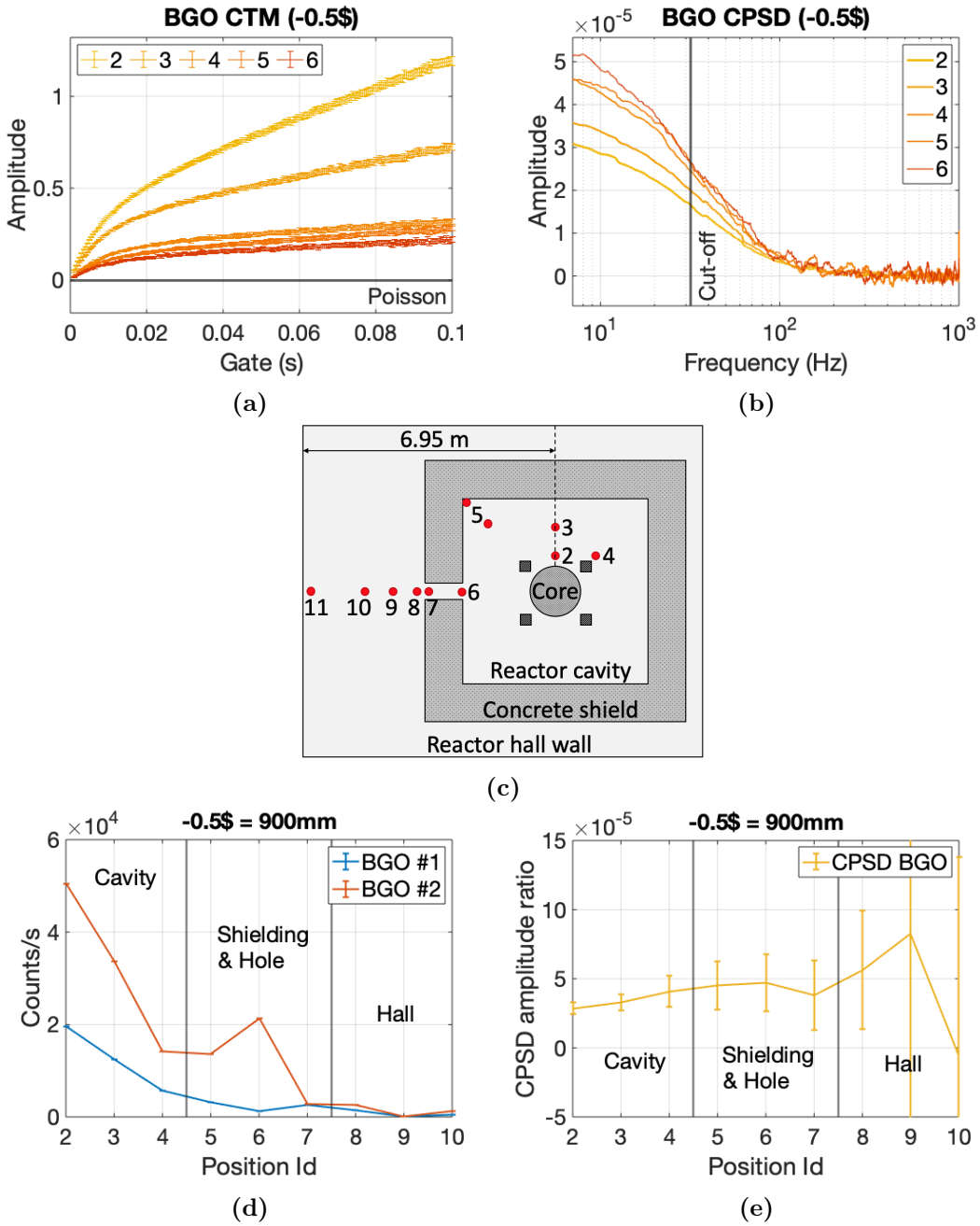

Figure 4.5: (a),(b): CTM and CPSD curves for several BGO distances from the core. The CTM curves are showing a non-poissonian behaviour and a clear cut-off frequency can be seen in CPSD curves. (d),(e): count rates and CPSD amplitude with respect to the BGO locations. The locations are reminded in (c).

From positions 8 to 10, the count rates at subcritical levels were too low for the CPSD amplitude to be larger than the white noise. For the farthest measurement -Position 11- it was thus chosen to operate at criticality for 2 hours to get the best statistics possible. At this distance of 6.85 m from the core center, correlated noise can be seen in Figure 4.6a and, in spite a lot of white noise, a cut-off frequency around 25 Hz -which is the expected value at critical according to Table 4.1- can be clearly identified in the CPSD from Figure 4.6b.

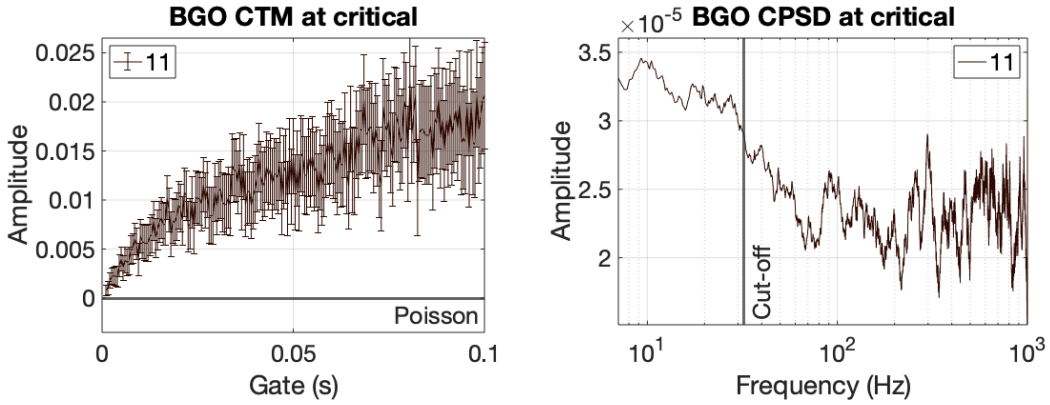

Figure 4.6: CTM (a) and CPSD (b) curves for BGO detectors at location 11.

The prompt gamma decay constants resulting from the fitting of the CTM and CPSD curves produced for each measurement of Table 4.2 are compared to the neutron noise reference data in Appendix M. For positions up to the cavity whole, constants are comparable to the reference for the -0.5$ subcritical state. For further distances, the measurements must be performed at critical for CTM or CPSD to show correlated noise. For the farthest BGO position possibly achievable in the CROCUS hall, a prompt decay constant within the 10% of the reference value is obtained (cf. Figure M.2). Hence, the limit in distance for gamma correlations measurements has not been found in CROCUS. As long as BGO scintillators were in direct line with the reactor vessel, gamma noise measurements may be achieved. This assumption will have to be validated or rejected by carrying further experimentations in other facilities.

Chapter 5

Summary and Outlook

Summary

The overall goal of the master thesis project was to improve the gamma field knowledge in the zero power reactor CROCUS from the full gamma field characterisation to specific applications such as zero power noise. LEAF, which consists in a gamma spectroscopy system, needed a characterisation in order to fulfil further research. All four scintillation detectors were thus calibrated in energy and efficiency, to be ready for experiments.

Measurements of in-core gamma spectra were performed, at different sub-critical and critical states of CROCUS, and compared to MCNP6.2 simulations and to a prompt U-235 spectrum produced with FREYA. The comparison of the experiments to MCNP6.2 enables the identification of resolved peaks of delayed processes not modelled by codes, such as the fission products Cs-137 and La-140. In the scientific community, a recent effort has been the determination of delayed gamma contributions. A new method allowing the estimation of local prompt to delayed gamma ratios in the reactor core has been developed. This technique estimates the delayed gamma fraction to be 0.30 ± 0.01 in the CROCUS control rod tubes, i.e. in the outer Umetal region of the core.

Neutron noise measurements, allowing for a non-invasive determination of the kinetic parameters of a reactor, is common practice. The first gamma and neutron-gamma correlations measurements in a reactor, though, were undertaken with the LEAF setup. $CeBr_3$ scintillators allowed for a precise and rapid reproduction of the prompt decay constant mean values measured with He-3 neutron detectors at different sub-critical and critical states in CROCUS and predicted with Serpent 2. Beyond these promising results, BGO scintillators which were selected for their high efficiency, provided us with gamma noise measurements at distances up to six meters from the reactor core centre, at critical (power 20 mW). At such distances, the multiple exponent CPSD fitting delivered α_p values comparable to the He-3 neutron measurements.

Outlook

The first in-core efficiency calibrated gamma spectra, and the new method providing delayed gamma fraction measurements, can lead to the determination of prompt to delayed gamma ratio as a function of the energy in CROCUS. This would complete the gamma field characterisation of the reactor's core.

In addition to its gamma spectroscopy capabilities, the LEAF system turns out to be an efficient gamma noise investigation device and future work on this topic could include:

- Extraction of other kinetic parameters, namely the effective delayed neutron fraction or the reactivity, which requires additional efforts on the in-core efficiency calibration.
- Estimation of kinetic parameters' uncertainties through stochastic methods such as bootstrapping, since the current uncertainty estimates are probably underestimated first order approximations.
- Application of gamma noise measurements with the LEAF system to other facilities and possibly industrial sites.
- Application of gamma noise to perturbation noise analysis which are conducted in the COLIBRI experiments.

Appendix A

Technical drawings of the LEAF detectors

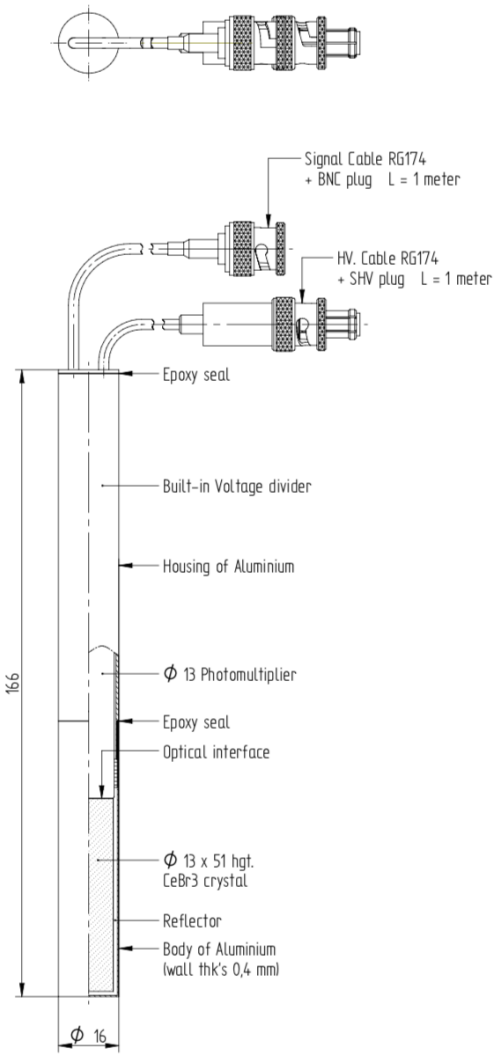

Figure A.1: Technical drawing of the $CeBr_3$ detector. The PMT is a Hamamatsu Type R12421.

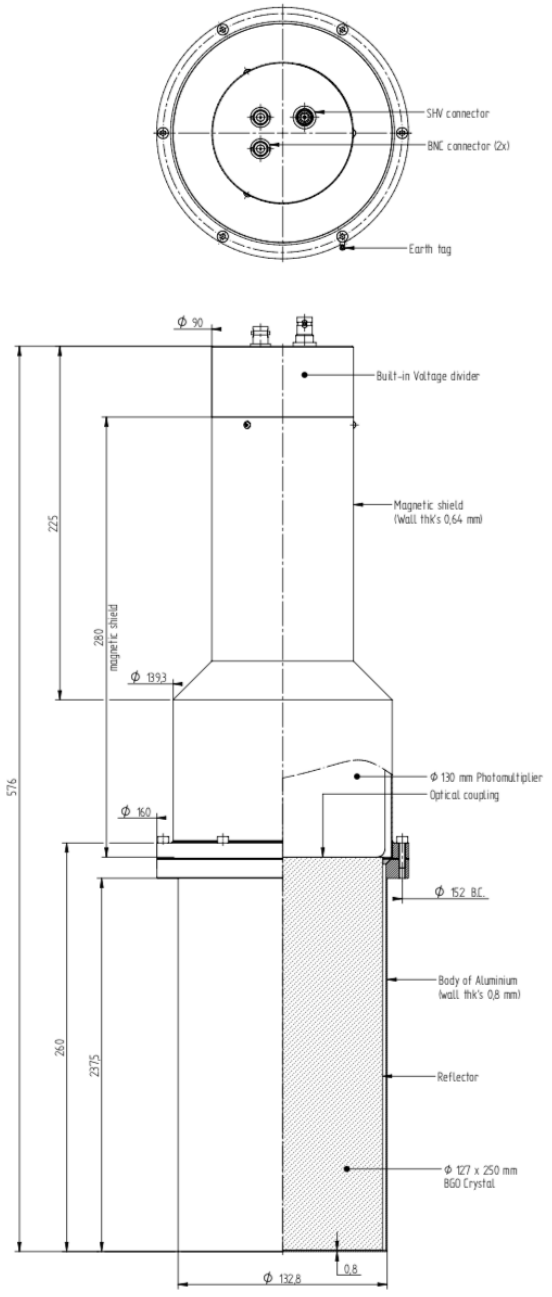

Figure A.2: Technical drawing of the BGO detector. The PMT is a Photonis 55 Type XP4578 PMT.

Appendix B

Energy calibration of the LEAF detectors

The linear calibrations for the LEAF detectors are presented Figures B.1 and B.2. The FWHM displayed on Figure B.3 are comparable to other crystals in literature, e.g. [26].

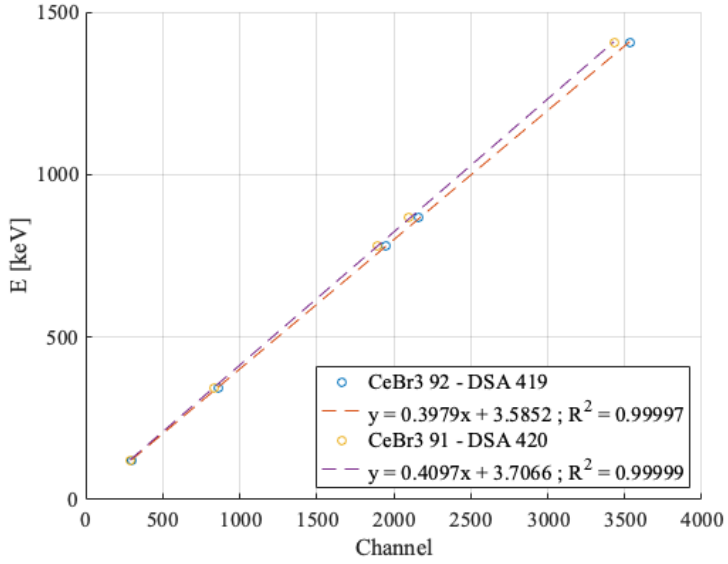

Figure B.1: Energy calibration results for the $CeBr_3$ detectors.

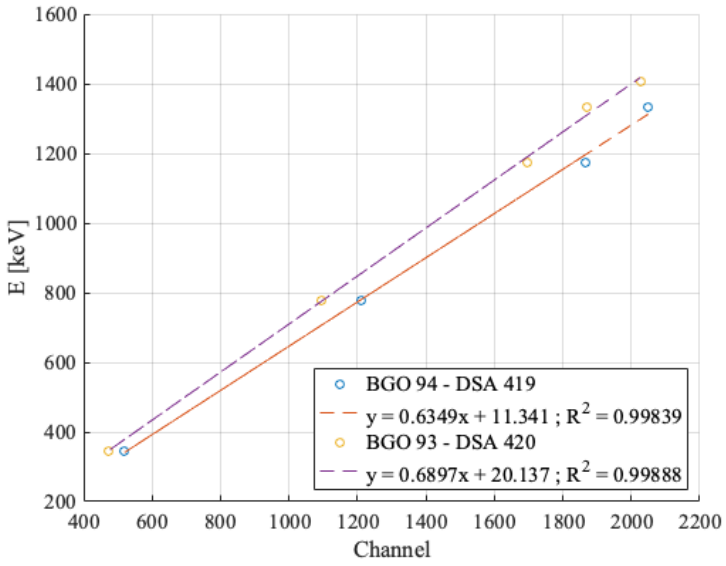

Figure B.2: Energy calibration results for the BGO detectors.

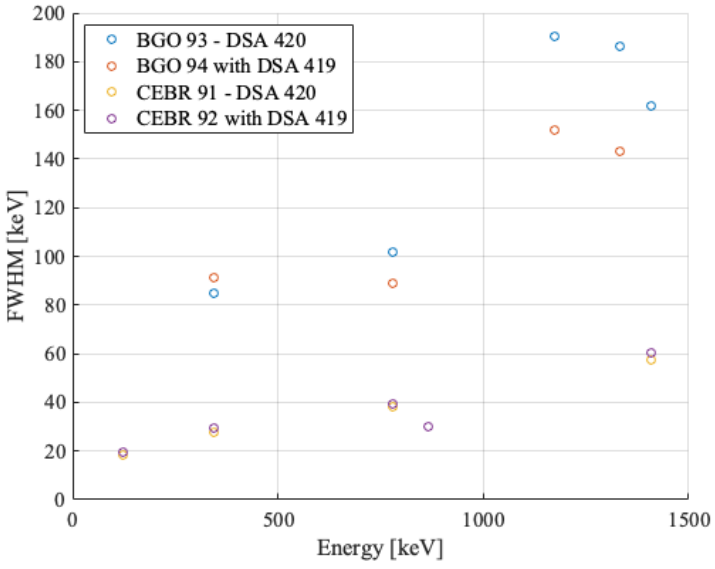

Figure B.3: FWHM for the LEAF detectors in dependence of energy, determined with standard Eu-152 and Co-60 sources.

Appendix C

Efficiency calibration setup for the LEAF detectors

The experimental setups for the source efficiency calibrations of the LEAF detectors are sketched Figures C.1 and C.2. As the geometry of the experiments has to be modelled with Serpent for simulations, we looked for the simplest design possible. The hanging strings do not affect photon transport and therefore only the detectors and sources have to be modelled.

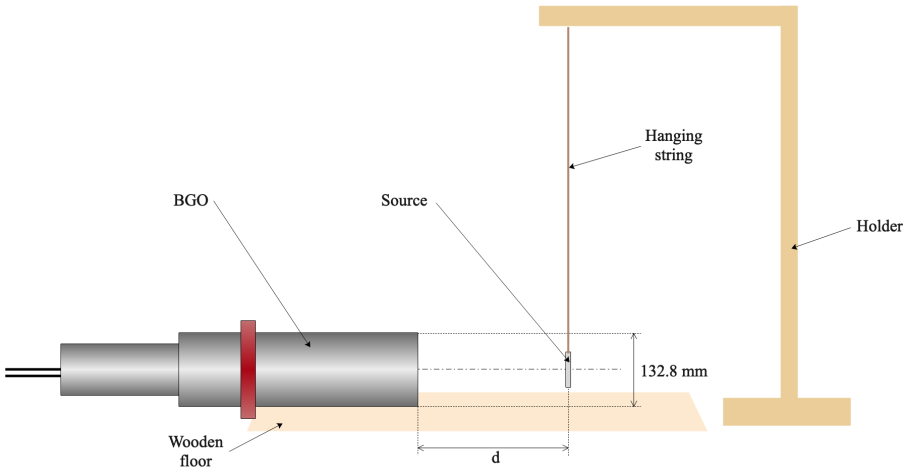

Figure C.1: Scheme of the efficiency calibration experimental setup for BGO scintillators.

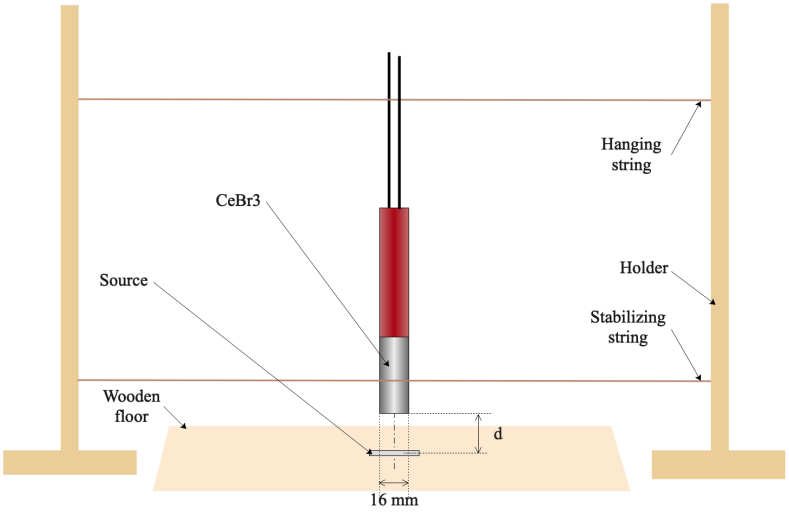

Figure C.2: Scheme of the efficiency calibration experimental setup for $CeBr_3$ scintillators.

Appendix D

LEAF detectors geometry in Serpent

Both $CeBr_3$ and BGO scintillators have been modelled with Serpent 2, Figures D.1a and D.1b, for efficiency calibrations with source and in-core. Dimensions are respecting the technical drawings from Appendix A.

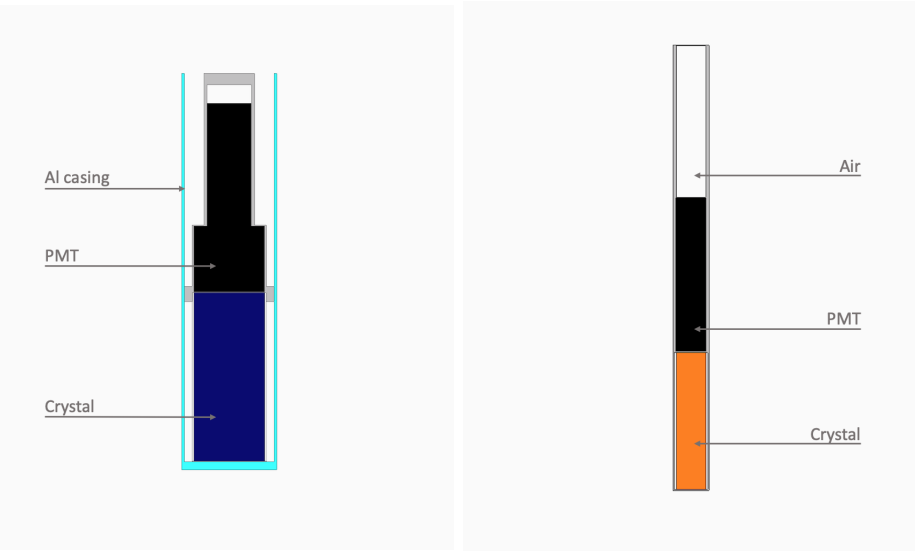

(a) BGO detector. **(b)** $CeBr_3$ detector.

Figure D.1: Serpent models of the LEAF detectors.

Appendix E

Scintillation detectors intrinsic efficiency

The gamma energy absorbed in the crystal is ([2], Chap 10):

$$E_a = N_1 \cdot h \cdot \bar{\nu_1} \tag{E.1}$$

where $h \cdot \bar{\nu_1} = \sum_i p_{E_i} \cdot E_i$ represents the average energy of the incident gammas, with the sum taken over all the emission rays of the gamma source.

The scintillation photon energy emitted in the crystal is ([2], Chap 10):

$$E_e = N_2 \cdot h \cdot \bar{\nu_2} \tag{E.2}$$

where:

- N_2: Number of scintillation photons.
- $h\bar{\nu_2} = \frac{hc}{\bar{\lambda_2}} = \frac{hc}{N_2} \int \frac{N_2(\lambda)}{\lambda} d\lambda$

with the integration taken over the entire scintillator emission spectrum.

From Equations E.1 and E.2, we can define the scintillation efficiency of the crystal as the ratio of the emitted energy over the absorbed one : $\epsilon_{crystal} = \frac{E_e}{E_a}$.

This crystal efficiency can be quickly approximated. According to [27], for a gamma energy deposition of $E_a = 1MeV$, in a $CeBr_3$ crystal, $N_2 = 45000$ luminous photons are created. This number of secondary photons produced N_2 is proportional to the energy

of the absorbed primary photon. It is also known from [28] that for $CeBr_3$, the emission spectrum is centered at $\bar{\lambda_2} = 380\ nm$ which corresponds to $h\bar{\nu_2} = 3.27eV$. As a result, $\epsilon_{CeBr_3} \approx \frac{N_2 \cdot h\bar{\nu_2}}{E_a} \approx 0.14$.
The same calculations, using numerical values from [29] and [5], lead to $\epsilon_{BGO} \approx 0{,}02$.

However, not all the scintillation photons will reach the photocathode but only a fraction $\eta = \frac{N_3}{N_2}$. If these photons are considered to be isotropically emitted inside the crystal, their probability to reach the photocathode has to be understood as the solid angle ratio $\frac{\Omega(M)}{4\pi}$, where $\Omega(M)$ represents the solid angle intercepting the photocathode surface from the interaction position M. This is valid only by neglecting the reflectors placed at the inner boundaries of the crystal.

The fraction η can be determined by integrating on the crystal volume:

$$\eta = \frac{1}{V} \int_V \frac{\Omega(M)}{4\pi} dV \tag{E.3}$$

If the crystal is a cylinder of radius R and height H:

$$\eta = \frac{1}{\pi R^2 H} \int_{r=0}^{R} \int_{z=0}^{H} \frac{\Omega(r,z)}{4\pi} 2\pi dr dz \tag{E.4}$$

where:

$$\Omega(r,z) = 2\pi \left(1 - \frac{z}{\sqrt{z^2 + r^2}}\right) \tag{E.5}$$

The expression of η presented Equation E.4 is not valid, as the gamma interactions are not uniformly distributed in the crystal, and the gamma mean free path in the crystal $\bar{l}$ should be introduced. The Equation E.4 becomes:

$$\eta = \frac{1}{\pi R^2 H} \int_{r=0}^{R} \int_{z=\sqrt{\bar{l}^2 - R^2}}^{\bar{l}} \frac{\Omega(r,z)}{4\pi} 2\pi dr dz \tag{E.6}$$

Then, the photomultiplier efficiency ϵ_{PMT} should be very close to 1. Indeed, secondary photons reaching the photocathode will induce a photoelectron which will be multiplied at the dynodes of the PMT and accelerated by the applied high voltage (Figure 2.2). At the output of the PMT, an electric pulse proportional to the energy of the event is produced, but the number of events is conserved: one emitted photoelectron should give one count

([2], Chap.10).

Eventually, the intrinsic efficiency can be written:

$$\epsilon_{int} = \frac{Counts}{N_1} = \underbrace{\frac{Counts}{N_3}}_{\epsilon_{PMT}} \cdot \underbrace{\frac{N_3}{N_2}}_{\eta} \cdot \frac{N_2}{E_e} \cdot \underbrace{\frac{E_e}{E_a}}_{\epsilon_{crystal}} \cdot \frac{E_a}{N_1} \tag{E.7}$$

The remaining terms can be derived from Equations E.1 and E.2 to obtain a more compact form:

$$\epsilon_{int} = \epsilon_{PMT} \cdot \eta \cdot \epsilon_{crystal} \cdot \frac{h\bar{\nu_1}}{h\bar{\nu_2}} \tag{E.8}$$

Appendix F

Efficiency calibration investigation for Bismuth Germanate detectors

The poor resolution of BGO scintillators prevent us from performing an efficiency calibration with an Eu-152 source as for $CeBr_3$ detectors. As pointed in Figure F.1, each peak gathers several gamma rays that are complex to identify. Indeed, the position of visible peaks on the spectrum do not always match the known gamma rays. For instance, on Figure F.1, we have a minimum right where the 964.1 keV peak should be. Even by trying to optimize this repartition of known gamma rays among the few visible peaks, the calculated absolute efficiencies were not consistent with the simulated curves displayed on Figure 2.8.

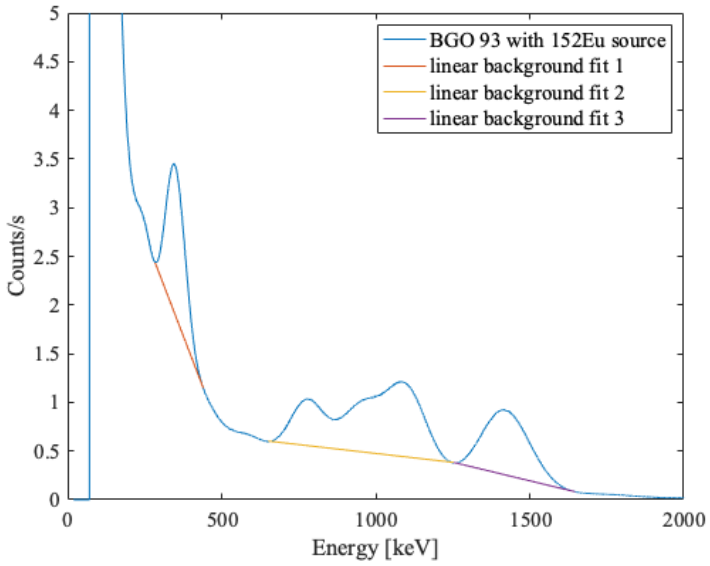

Figure F.1: Eu-152 spectrum acquire with BGO #1.

These first experiments with a classic Eu-152 source pointed out the need for "single-peak" sources not to make mistakes computing the area N(E). Some gold and indium dosimeter used for the PETALE experiment [30] primary measurements allow us to take advantage

of the ^{197}Au(n,γ)^{198}Au and the ^{115}In(n,γ)^{116m1}In reactions producing a single 411.8 keV gamma peak for gold and a 1097.3 keV and 1294.5 keV double-peak for Indium [31].

The samples were activated thanks to the Pu Be neutron source from the CAROUSEL facility [32]. Then, the samples' activity (Equation F.1) was determined using the LOTUS HPGe from the spectroscopy lab of the EPFL.

$$A(t_0) = \frac{N(E)}{\Delta t_{HPGe} \cdot \epsilon_{HPGE}(E) \cdot p_E} \tag{F.1}$$

where:

- $A(t_0) = A_0$: Activity of the source right after the HPGe measurement.
- $N(E)$: Net peak area at the energy E, obtained from the measured spectrum.
- P_E: Probability that the gamma is emitted with an energy E. (put ref of nuclides table)
- $\epsilon_{HPGE}(E)$: LOTUS HPGe absolute efficiency at the energy E with the source at the standard measurement distance.
- Δt_{HPGe}: Measurement time inside the HPGe.

The activity of the samples known precisely, measurements as depicted in Appendix C, with both BGO and with samples at distances $d = [4; 6; 9; 16]cm$, have been conducted. Since the isotopes ^{198}Au and ^{116m1}In have short half-lives, respectively 2.7 days and 54 min, the activity of the samples can't be considered as constant during the experiments and the formula presented on Equation 2.2 can't be used.

A method taking care of the source activity change during the measurements with BGO detectors is presented below:

At time t_0, the number of nuclei in the sample that are to decay is :

$$N_0 = \frac{A_0}{\lambda} \tag{F.2}$$

When we start the measurement with the BGO, this number becomes:

$$N_{start} = N_0 \cdot e^{-\lambda(t_{start} - t_0)} \tag{F.3}$$

Similarly, at the end of the measurement:

$$N_{stop} = N_{start} \cdot e^{-\lambda \cdot \Delta t_{experiment}} \tag{F.4}$$

Since a gamma is emitted per decay, the number of gammas emitted during the experiment is:

$$N_{emitted} = N_{start} - N_{stop} = N_0 \cdot e^{-\lambda(t_{start}-t_0)} \cdot \left(1 - e^{-\lambda \cdot \Delta t_{experiment}}\right) \tag{F.5}$$

On the other hand, the number of counts under the gamma peak at energy E in the measured spectrum is:

$$N_{BGO}(E) = N_{emitted} \cdot p_E \cdot \epsilon_{abs\ BGO}(E) \tag{F.6}$$

So the absolute efficiency can be deduced:

$$\epsilon_{abs}(E) = \frac{N_{BGO}(E)}{N_{emitted} \cdot p_E} = \frac{N_{BGO}(E)}{N_0 \cdot e^{-\lambda(t_{start}-t_0)} \cdot \left(1 - e^{-\lambda \cdot \Delta t_{experiment}}\right) \cdot p_E} \tag{F.7}$$

If the quantity $\lambda \cdot \Delta t_{experiment} << 1$, we can perform a Taylor expansion of the exponential function in the neighborhood of 0:

$$\epsilon_{abs}(E) = \frac{N_{BGO}(E)}{N_{emitted} \cdot p_E} = \frac{N_{BGO}(E)}{N_0 \cdot e^{-\lambda(t_{start}-t_0)} \cdot \lambda \cdot \Delta t_{experiment} \cdot p_E} \tag{F.8}$$

$$\epsilon_{abs}(E) = \frac{N_{BGO}(E)}{A(t_{start}) \cdot \Delta t_{experiment} \cdot p_E} \tag{F.9}$$

We finally obtain Equation F.9 the classic expression from Equation 2.2, which prove the validity of this method.

In Figure F.2 is displayed the single 411 keV gamma peak from ^{197}Au(n,γ)^{198}Au reaction for samples at distances $d = [4; 6; 9; 16]cm$. Linear background filters can also be seen. Regarding the spectra obtained with activated Indium foils Figure F.3, they are not "clean" enough to be used. In order to still get absolute efficiency values around 1 MeV, a Na-22 source was used since it has two spaced-enough gamma rays at 511 keV and 1275 keV (Figure F.4).

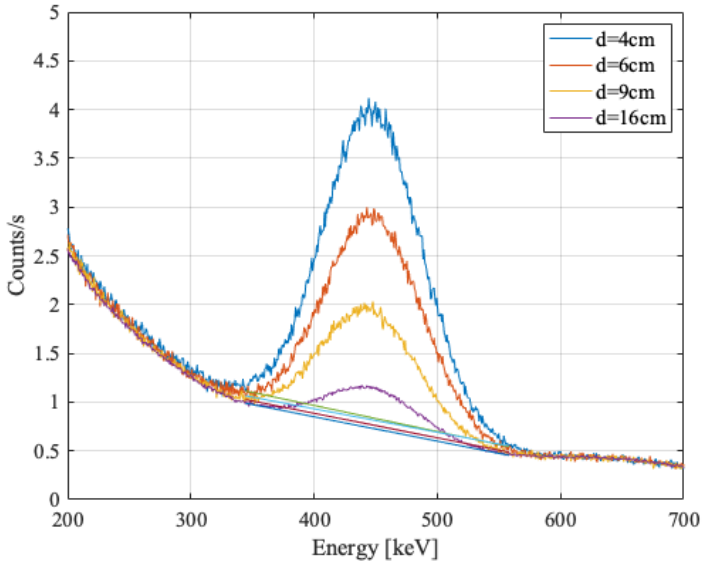

Figure F.2: Activated gold spectra acquired with BGO #1.

On Table F.1 and Table F.2 can be found the measured absolute efficiency values for BGO #1 and #2 while on Table F.3 are shown the geometric values simulated thanks to Serpent. It appears that the ϵ_{abs} values for BGO are one order of magnitude higher than for the $CeBr_3$ detectors, even if for BGO crystals $\epsilon_{BGO} \approx 0.02 < \epsilon_{CeBr3}$. In addition to that, the ratio $\frac{\epsilon_{abs}}{\epsilon_{geom}}$ does not provide constant values of ϵ_{int} as for $CeBr_3$ detectors. The physical process in a crystal that large must definitely be different.

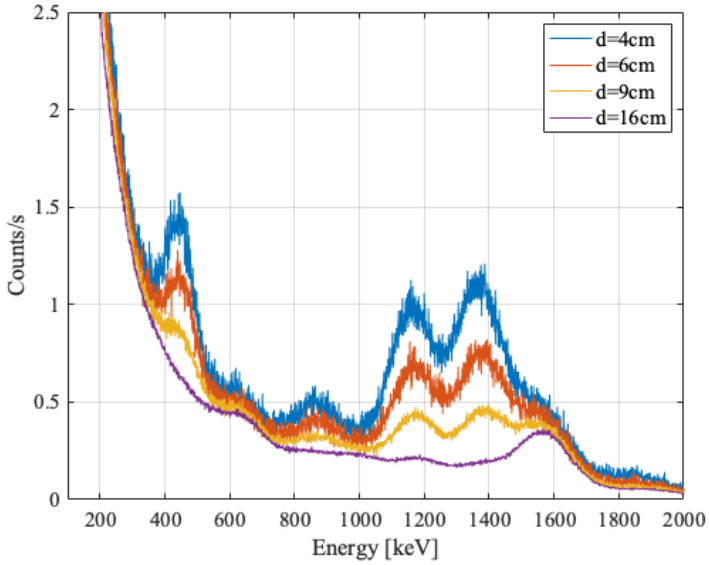

Figure F.3: Activated indium spectra acquired with BGO #1.

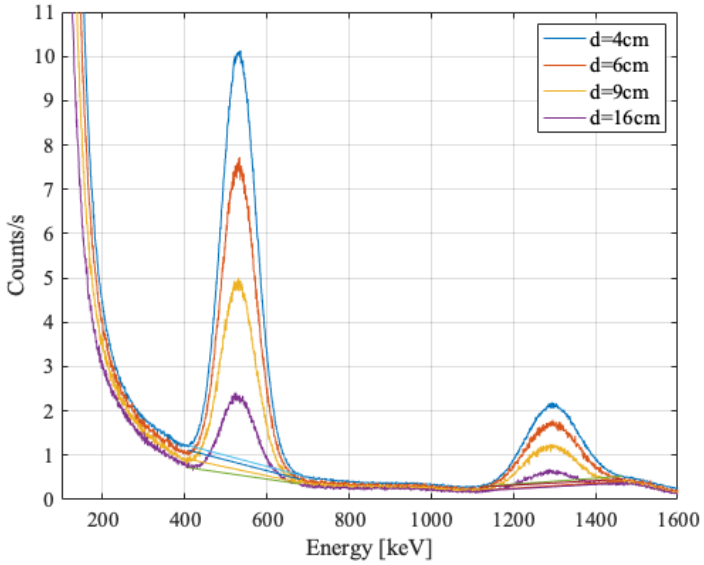

Figure F.4: Na-22 spectrum acquired with BGO #1.

Table F.1: Measured absolute efficiencies for BGO #1

d (cm)	ϵ_{abs} (411 keV)	ϵ_{abs} (511 keV)	ϵ_{abs} (1275 keV)
4	0.1569(63)	0.1290(2)	0.0650(2)
6	0.1023(41)	0.0933(2)	0.0498(2)
9	0.0590(23)	0.0587(1)	0.0330(1)
16	0.0189(8)	0.0248(1)	0.0107(1)

Table F.2: Measured absolute efficiencies for BGO #2

d (cm)	ϵ_{abs} (411 keV)	ϵ_{abs} (511 keV)	ϵ_{abs} (1275 keV)
4	0.1494(60)	0.1269(3)	0.0633(3)
6	0.1084(44)	0.0985(2)	0.0500(2)
9	0.0827(33)	0.0576(1)	0.0336(1)
16	0.0338(14)	0.0238(3)	0.0133(1)

A first comparison of the measured and simulated efficiencies for BGO scintillators is displayed Figure F.5. The experimental efficiency points are altogether consistent. Indeed, the efficiency is decreasing while increasing the source distance or the gamma-ray energy. (except the 511 keV value for the BGO #1 at d=16 cm). Still, three points are not enough to get a preview of what should be the physical trend. All theoretical efficiency coefficients presented in Section 4.3 must have an energy dependence in scintillation crystals of that size.

Table F.3: Simulated geometric efficiencies for BGO detectors

d (cm)	ϵ_{geom} (411 keV)	ϵ_{geom} (511 keV)	ϵ_{geom} (1275 keV)
4	0.12209(7)	0.11960(9)	0.09390(8)
6	0.0834(6)	0.08260(7)	0.06540(6)
9	0.05213(5)	0.05128(10)	0.04146(9)
16	0.02228(3)	0.02214(4)	0.01872(4)

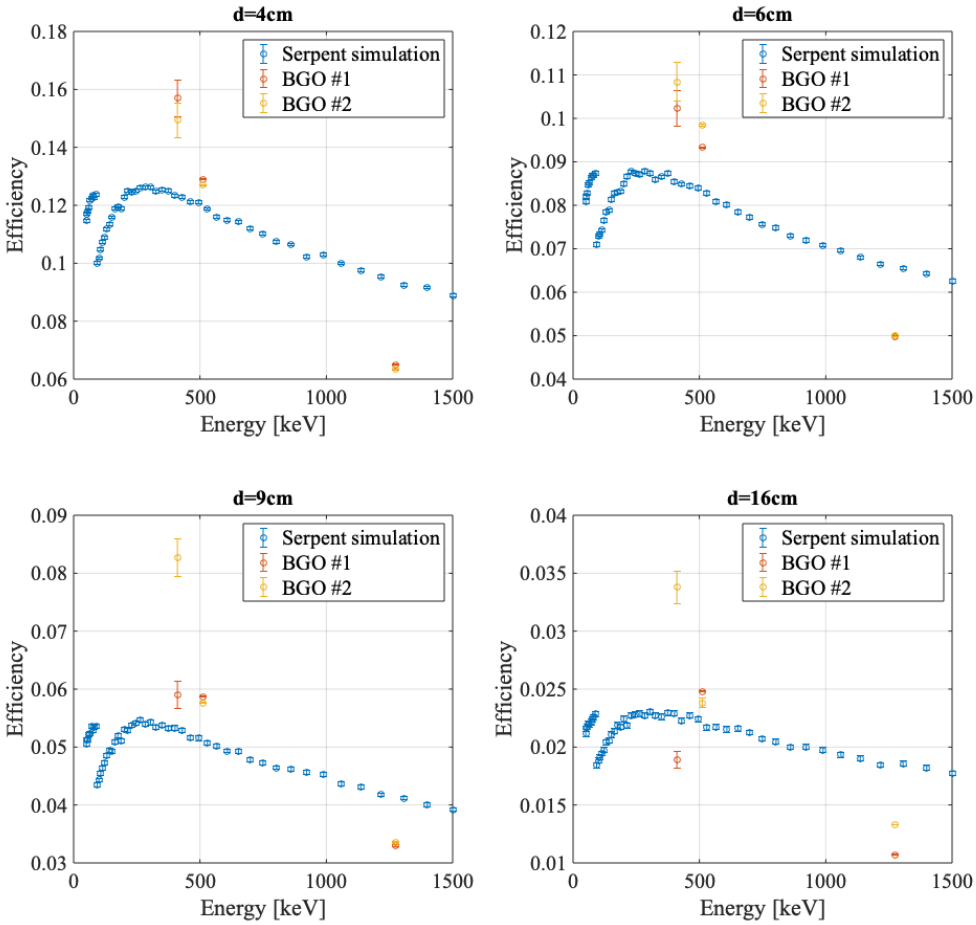

Figure F.5: Comparison of the measured and simulated efficiencies for the BGO detectors

Appendix G

Simulated geometric efficency curves for several CROCUS core configurations

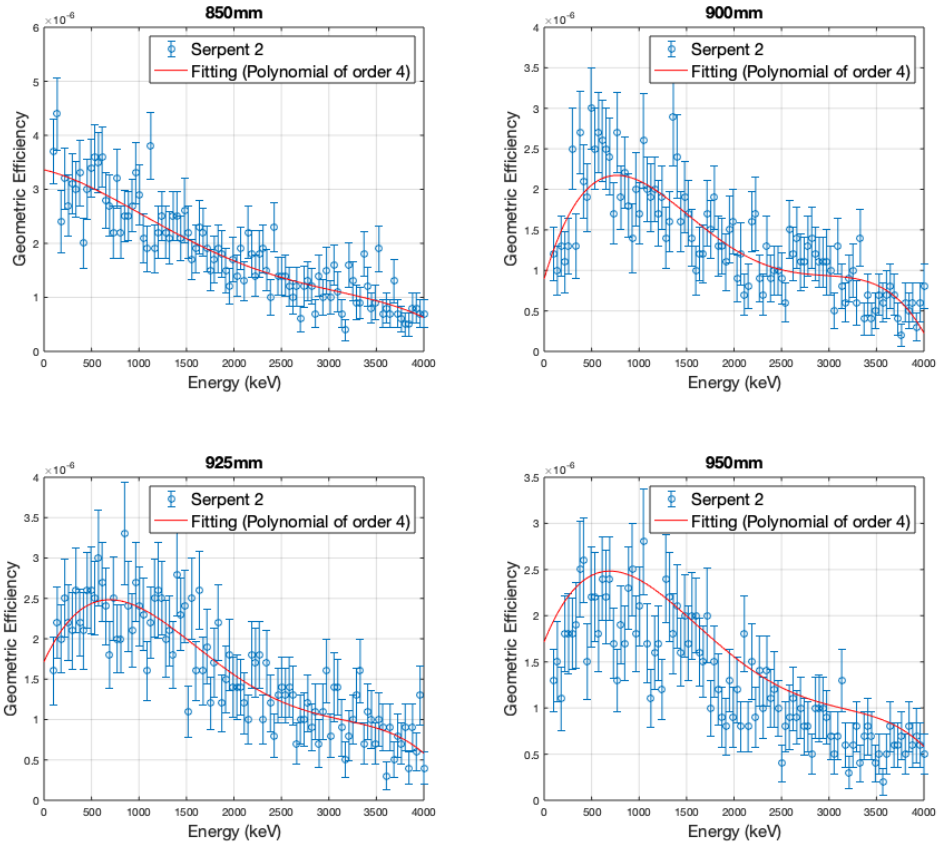

Figure G.1: Geometric efficiency curves for four different CROCUS subcritical states. These curves are the result of Serpent simulations.

Appendix H

Nuclear reactor kinetics theory

The following derivations are adapted from Prof. Dr. Piero Ravetto's reactor physics lectures given at Politecnico di Torino for the Master of Science program in nuclear engineering.

H.1 Time dependent Boltzmann transport equation

A neutron distribution ϕ in a reactor at time t, direction $\boldsymbol{\Omega}$, energy E and position $\boldsymbol{r}$ can be described by the linear Boltzmann equation, as a balance equation between losses and sources S:

$$\begin{aligned}\left[\frac{1}{v}\frac{\partial}{\partial t}+\Sigma(\boldsymbol{r},E)+\boldsymbol{\Omega}\cdot\overrightarrow{\nabla}\right]\phi(\boldsymbol{r},E,\boldsymbol{\Omega},t)=S(\boldsymbol{r},E,\boldsymbol{\Omega},t)\\ +\int dE'\oint d\Omega'\Sigma_s(\boldsymbol{r},E')f_s(\boldsymbol{r},E'\rightarrow E,\boldsymbol{\Omega'}\cdot\boldsymbol{\Omega})\phi(\boldsymbol{r},E',\boldsymbol{\Omega'},t)\\ +(1-\beta)\int dE'\oint d\Omega'\nu\Sigma_f(\boldsymbol{r},E)\frac{\chi_p(\boldsymbol{r},E)}{4\pi}\phi(\boldsymbol{r},E',\boldsymbol{\Omega'},t)\\ +\sum_{i=1}^{R}\frac{\chi_i(\boldsymbol{r},E)}{4\pi}\lambda_i C_i(\boldsymbol{r},t)\end{aligned} \tag{H.1}$$

with the initial condition $\phi(\boldsymbol{r},E,\boldsymbol{\Omega},t=0)$, a null incoming flux boundary condition $\phi(\boldsymbol{r_s},E,\boldsymbol{\Omega_{in}},t)=0$ and where:

- v is the neutron velocity;
- Σ the macroscopic cross section;
- β the delayed neutron fraction;
- β_i refers to the probability that the fission product i is produced in a fission and that this product will produce one delayed neutron, with $\sum_{i=1}^{R}\beta_i=\beta$;

- λ_i is the decay constant of the precursor i;
- $C_i(\boldsymbol{r},t)$ the quantity of precursor i per unit volume at point $\boldsymbol{r}$ and at time t;
- $\lambda_i C_i(\boldsymbol{r},t)$ the number of neutrons emitted by the precursor i per unit volume and time at the point $\boldsymbol{r}$.

In order to solve the neutron transport equation with delayed neutrons, the evolution of the precursor density C_i must be known :

$$\frac{\partial C_i(\boldsymbol{r},t)}{\partial t} = -\lambda_i C_i(\boldsymbol{r},t) + \beta_i \int dE' \oint d\Omega' \nu \Sigma_f(\boldsymbol{r},E')\phi(\boldsymbol{r},E',\boldsymbol{\Omega'},t) \tag{H.2}$$

The following operators are introduced:

$$\hat{\boldsymbol{L}} \equiv \int dE' \oint d\Omega' \Sigma_s(\boldsymbol{r},E') f_s(\boldsymbol{r},E' \to E,\boldsymbol{\Omega'}\cdot\boldsymbol{\Omega})v' - \Sigma(\boldsymbol{r},E')v' - v'\boldsymbol{\Omega'}\cdot\boldsymbol{v} \tag{H.3}$$

$$\hat{\boldsymbol{M_p}} \equiv (1-\beta)\int dE' \oint d\Omega' \nu \Sigma_f(\boldsymbol{r},E)\frac{\chi_p(\boldsymbol{r},E)}{4\pi} \tag{H.4}$$

$$\hat{\boldsymbol{M_i}} \equiv \beta_i \int dE' \oint d\Omega' \nu \Sigma_f(\boldsymbol{r},E)\frac{\chi_i(\boldsymbol{r},E)}{4\pi} \tag{H.5}$$

with $\hat{\boldsymbol{M}} = \hat{\boldsymbol{M_p}} + \sum_{i=1}^{R} \hat{\boldsymbol{M_i}}$.

to simplify Equations H.1 and H.2 as follows:

$$\frac{\partial n(\boldsymbol{r},E,\boldsymbol{\Omega},t)}{\partial t} = \hat{\boldsymbol{L}}n + \hat{\boldsymbol{M_p}}n + \sum_{i=1}^{R}\lambda_i\epsilon_i + S \tag{H.6}$$

$$\frac{\partial \epsilon_i(\boldsymbol{r},E,t)}{\partial t} = \hat{\boldsymbol{M_i}}n - \lambda_i\epsilon_i \tag{H.7}$$

The neutron density n is preferred the neuron flux ϕ and the delayed neutron emissivity is defined as $\epsilon_i(\boldsymbol{r},E,t) = \frac{\chi_i(\boldsymbol{r},E)}{4\pi}C_i(\boldsymbol{r},t)$ with $i \in [\![1,R]\!]$. One can notice that the emissivity does not depend on $\boldsymbol{\Omega}$ since the emission of delayed neutrons is isotropic.

H.2 Point kinetics equations

If the independance of the neutron density with respect to space and energy can be assumed, point kinetics equations can be derived from the general neutron transport equation.

First, we introduce the separability of the neutron density into a time dependent amplitude A and space and energy dependent shape function φ:

$$n(\boldsymbol{r},E,\boldsymbol{\Omega},t) = A(t)\varphi(\boldsymbol{r},E,\boldsymbol{\Omega},t) \tag{H.8}$$

and we inject it into the Transport and Emissivity Equations H.6 and H.7 to obtain the Shape Equations:

$$\frac{dA(t)}{dt}\varphi + A(t)\frac{d\varphi}{dt} = A(\hat{\boldsymbol{L}} + \hat{\boldsymbol{M}}_{\boldsymbol{p}})\varphi \sum_{i=1}^{R} \lambda_i \epsilon_i + S \tag{H.9}$$

$$\frac{\partial \epsilon_i}{\partial t} = A\hat{\boldsymbol{M}}_{\boldsymbol{i}}\varphi - \lambda_i \epsilon_i \tag{H.10}$$

With the initial conditions $n(\boldsymbol{r},E,\boldsymbol{\Omega},t=0) = N_0(\boldsymbol{r},E,\boldsymbol{\Omega})$ and $\epsilon_i(\boldsymbol{r},E,t=0) = \frac{\hat{\boldsymbol{M}}_{\boldsymbol{i0}} N_0}{\lambda_i}$, the Shape Equations system provides us with the reference system $(\hat{\boldsymbol{L}}_{\boldsymbol{0}} + \hat{\boldsymbol{M}}_{\boldsymbol{0}})N_0$ with $N_{0,boundary}(\boldsymbol{\Omega_{in}})$.

If we integrate the Shape Equations over energy, direction and position with a weighted function w like this: $\int \boldsymbol{dr} \oint d\Omega \int dE \varphi(\boldsymbol{r},E,\boldsymbol{\Omega}) w(\boldsymbol{r},E,\boldsymbol{\Omega}) = (w,\varphi)$, we obtain a balance on weighted particles. Since we would like to take into account the importance (ref adjoint problem) of each neutron, the initial neutron importance density $N_0^\dagger$ from the adjoint reference system seems to be the best candidate for w.

Eventually, we project the shape equations on $w = N_0^\dagger$ to get the Point Kinetic Equations:

$$\frac{dA}{dt} = \frac{\rho - \tilde{\beta}}{\Lambda} A + \sum_i \lambda_i C_i + S \tag{H.11}$$

$$\frac{dC_i}{dt} = \frac{\tilde{\beta}_i}{\Lambda} A - \lambda_i C_i \tag{H.12}$$

with $C_i = \frac{(N_0^\dagger, \epsilon_i)}{\Lambda F}$.

where:

- $F = (N_0^\dagger, \hat{\boldsymbol{M}}\varphi)$: total importance associated to the shape of the flux.
- $\rho = \frac{(N_0^\dagger, \boldsymbol{\delta}\hat{\boldsymbol{H}}\varphi)}{F}$: reactivity.
- $\tilde{\beta} = \frac{(N_0^\dagger, \sum_{\boldsymbol{i}} \hat{\boldsymbol{M}}_{\boldsymbol{i}}\varphi)}{F}$: effective delayed neutron fraction.
- $\Lambda = \frac{(N_0^\dagger, \varphi)}{(N_0^\dagger, \hat{\boldsymbol{M}}\varphi)}$: prompt generation time.

Appendix I

Rossi-α auto correlation function investigations

In order to produce Rossi distributions from the signals obtained with 500 μs dwell time, the "xcorr" Matlab inner cross correlation function was used. The results obtained for gamma correlation measurements of 2h with both $CeBr_3$ at five CROCUS subcritical states and at criticality are displayed Figure I.1. Since the main part of the decay is happening in 0.01s, the fit only relies on 20 points. In order to get more points for a better fitting we need to reduce the dwell time far under 500 μs, which must lead to data size handling problems and too long calculation time.

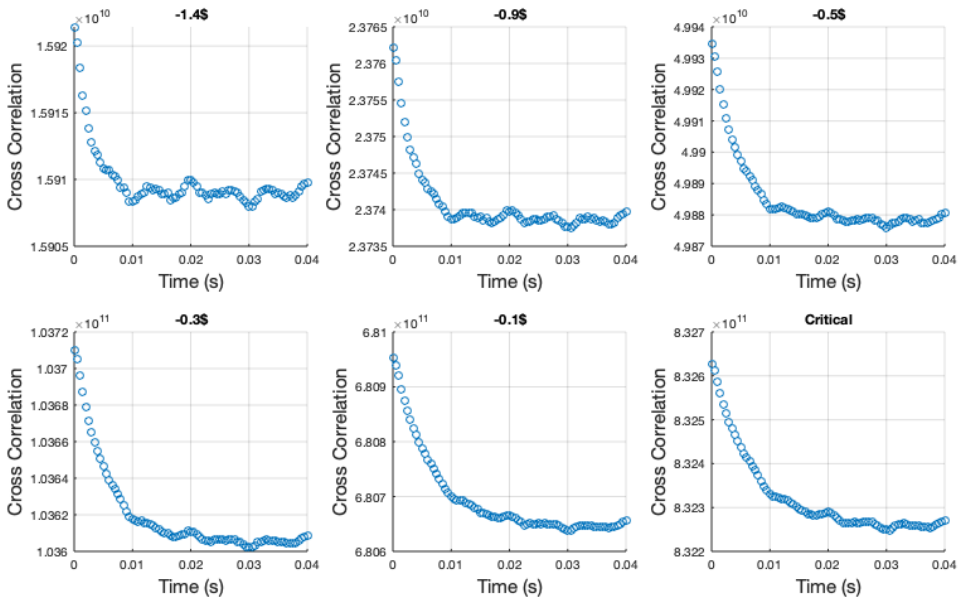

Figure I.1: Rossi-*alpha* curves obtained with $CeBr_3$ correlation measurements.

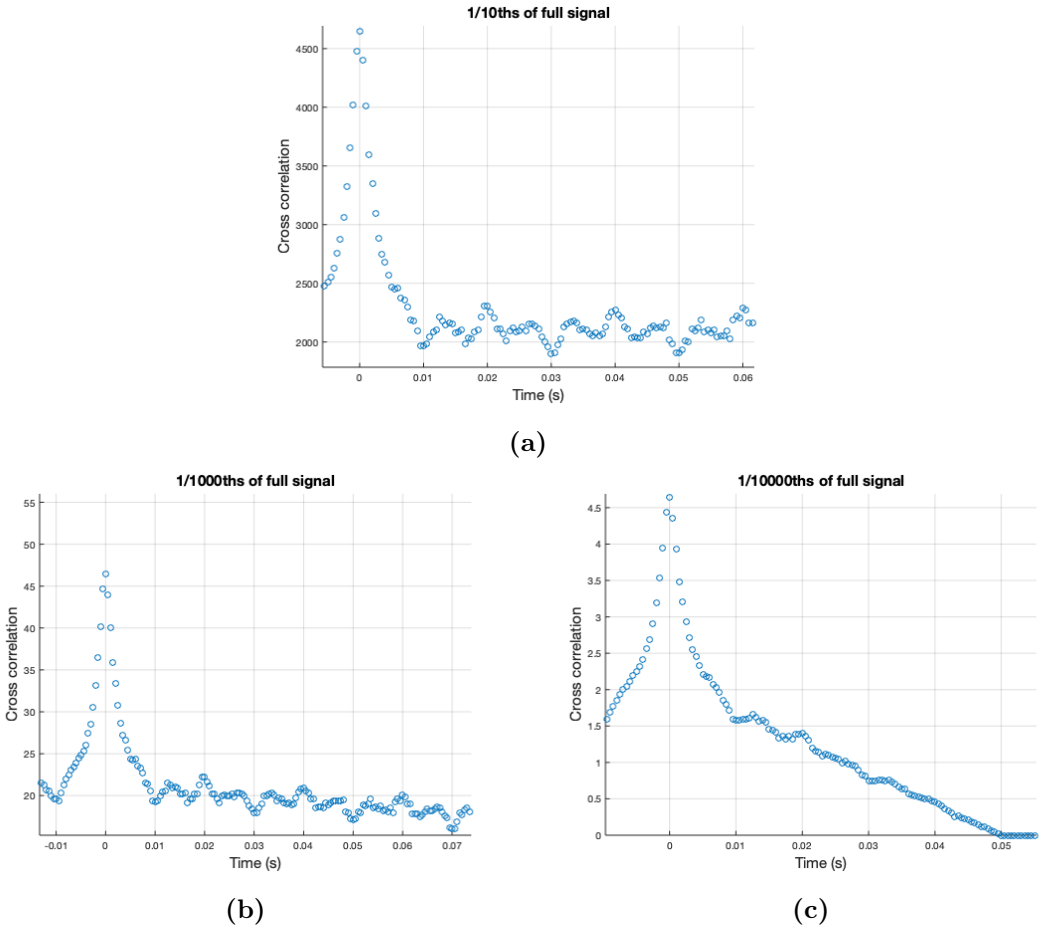

Figure I.2: Cross correlations obtained by applying the segmenting and averaging method to the full signal with different segment lengths.

Trying to avoid such problems, the Bartlett method used for PSDs was adapted to the cross correlation function. Cross correlations were performed on segments of length ten time shorter than the full signal at first, and on 10000ths of the full signals. The resulting averaged cross correlation curves are shown Figures I.2a, I.2b and I.2c . A linear trend can be observed for short segment lengths. This is slightly visible in Figure I.2b and obvious in Figure I.2c. In order to understand this phenomenon, artificial signals of the same length as our real measurements were produced using the white Gaussian noise to signal generator Matlab function "awgn". the same PSD analysis was then conducted on these signals and the results are presented in Figure I.3. The expected Dirac signal is visible at the origin but the same linear effect as with the real signals is visible. It appears that for too short segments the Dirac can not be properly seen but only a Dirac-approximated triangle. This effect can be avoided by applying standardization to the full signal before welching (Figure I.4), but it adds noise to the ground line especially around the origin.

Finally, the standardization was applied to the $CeBr_3$ gamma correlation measurements. The cross correlation functions were calculated on full signals and also on segments so as to average it. The cross correlation function exponential decays were fitted with multiple

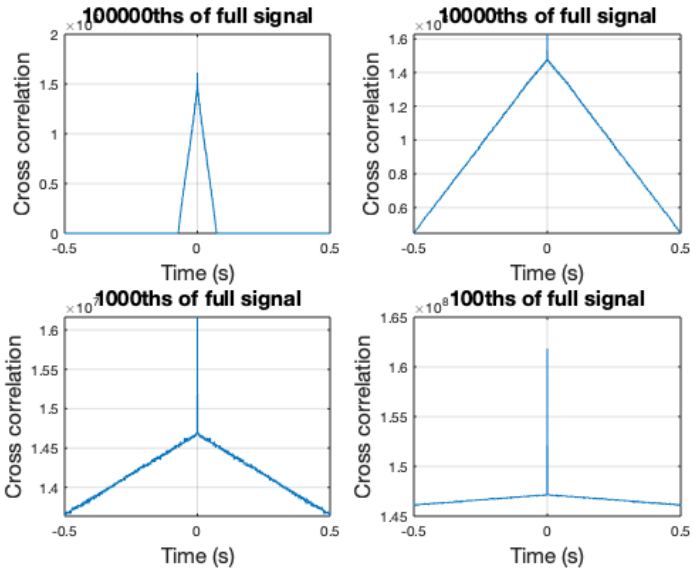

Figure I.3: Averaged cross correlation curves, produced with several segment lengths, from artificial signals.

exponents and the resulting prompt decay constant for each CROCUS core configuration are shown Figure I.5. Judging from these results, it is not worth segmenting and averaging as the shorter the segments, the larger the overestimation of α. Cross correlation on the full signal is also providing overestimated decay constants at deep subcritical compared to the PSD which must carry the same information. As a result, PSD curves, which fitting results are closer to the reference prompt decay constants, should be preferred to auto or cross correlation functions.

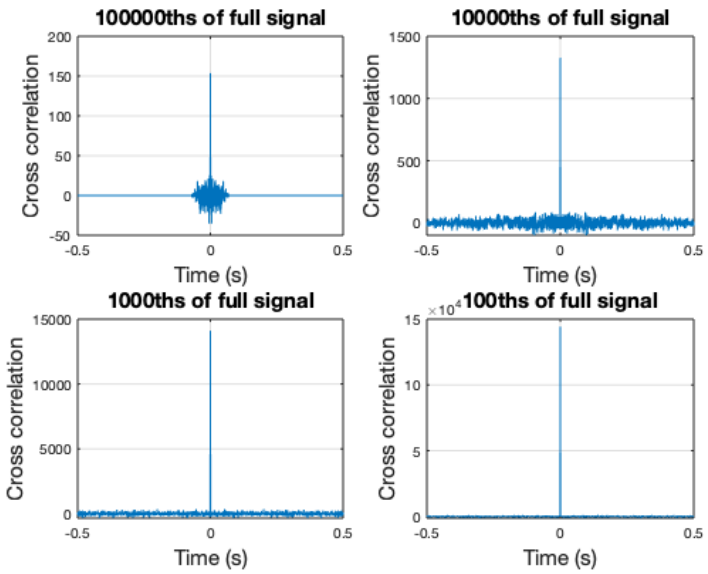

Figure I.4: Averaged cross correlation curves, produced with several segment lengths, from standardized artificial signals.

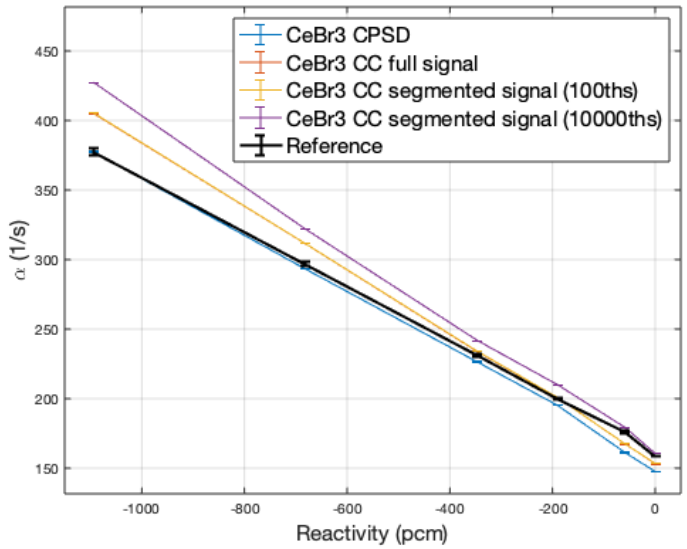

Figure I.5: CPSD and Cross correlation prompt decay constants as function of reactivity.

An additional argument against the fitting of the cross correlation function stands in Figure I.6 displaying the cross correlation curve fitting along with its residuals function. In the residuals a 20ms periodic oscillation corresponding to the 50Hz frequency is observable. The cross correlation function is therefore not an exponential but is always oscillating around it. The resulting uncertainty on the decay constant will be larger by fitting the cross correlation function than by fitting the PSD where the 50Hz contribution can be removed by cutting out the corresponding spike.

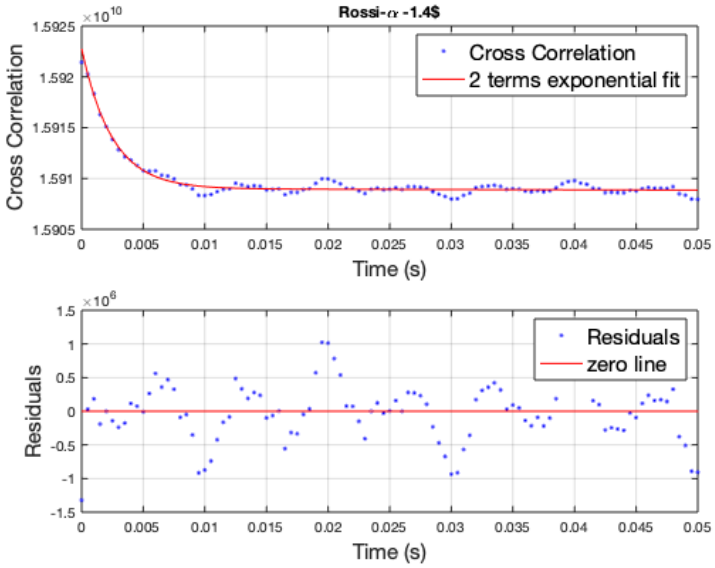

Figure I.6: Cross correlation curve fitting example.

Appendix J

Threshold investigation for $CeBr_3$ correlation measurements

Establishing the optimal threshold for BF_3 neutron detector is fairly direct by analysing the pulse height spectrum of the detector. A clear limit between low energy pulses (gamma rays or noise) and Li-7 and α energy deposition from MeV to 2.79 MeV can be observed. The threshold is to be set to discriminate out pulses at energy lower than 0.84 MeV which are not induced by neutrons. The threshold was set to 0,5V for our two BF_3 detectors.

For $CeBr_3$ scintillators, the spectrum being a decaying exponential, there is no clear limit between noise or X-rays and gamma rays of importance. A more thorough study on how the threshold affects the correlation measurements need to be carried out. To this purpose, gamma correlation measurements of 30min were acquired with $CeBr_3$ scintillators threshold varying from 0.0V to 1.0V, corresponding to energies from 0 to 1.1 MeV. The PSD and CPSD curves for each of these measurements are shown Figures J.1a and J.1b.

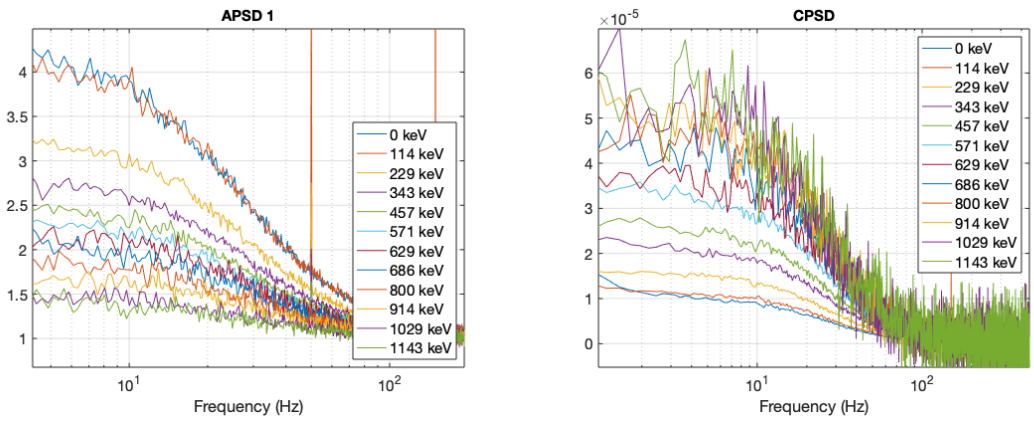

(a) **(b)**

Figure J.1: APSD and CPSD curves obtained with $CeBr_3$ detectors for thresholds from 0 to 1.1 MeV. APSD curves have been normalised to their respective high energy mean values.

The higher the threshold, the lower the amplitude of the APSD curves. The same phenomenon was observed with neutron noise since with BF_3 increasing the threshold only reduces the effective amount of counts seen by the detector and therefore the amplitude of the curve. Indeed, with BF_3 detectors we just count the neutrons at the origin of the (n,p) reactions, and we miss the information on their energy, while with $CeBr_3$ scintillators, we detect gamma-rays from low and high energies and increasing the threshold mean filtering low energy gammas. On the contrary, the amplitude of the CPSD is increasing with threshold, which suggests that the correlated information is contained in the high energy events detected. Low energy event cut out from the spectrum are not likely to be gammas from a fission chain that have travelled through the whole core from one detector to the other. With CPSD we are looking at whole core while in APSD we are looking at a local behaviour where low and high energy gammas have all the same importance.

As a result a trade-off is to be made between count rate and amplitude while considering CPSD, as depicted by Figure J.2. The best threshold for our correlation measurements is 0.1V and corresponds to 114 keV on the spectrum. A high count rate is privileged over the amplitude, which is already high enough to allow for a precise fitting. Figure J.3 shows that 0.1V threshold is providing us with the most accurate CPSD fit result for the prompt gamma decay constant α, with the smallest uncertainty.

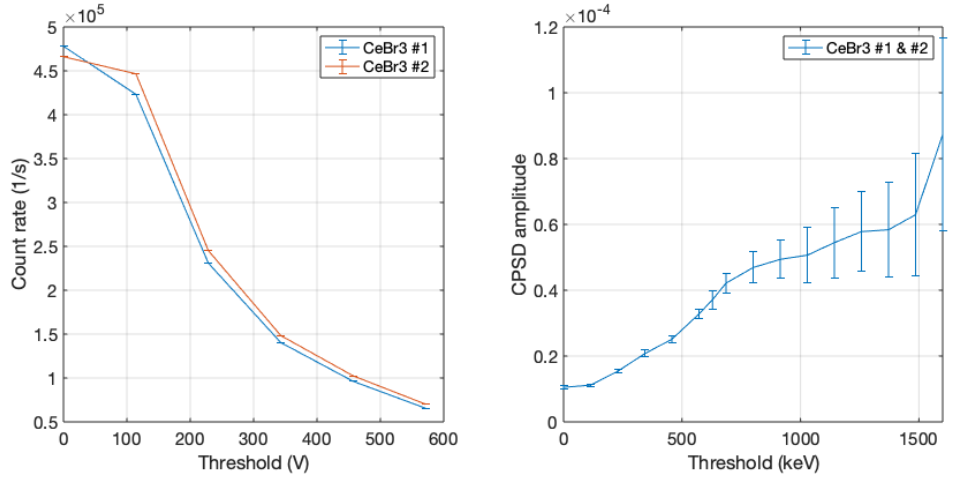

Figure J.2: Prompt gamma constant and its relative uncertainty as function of the measurement duration, for several $CeBr_3$ thresholds.

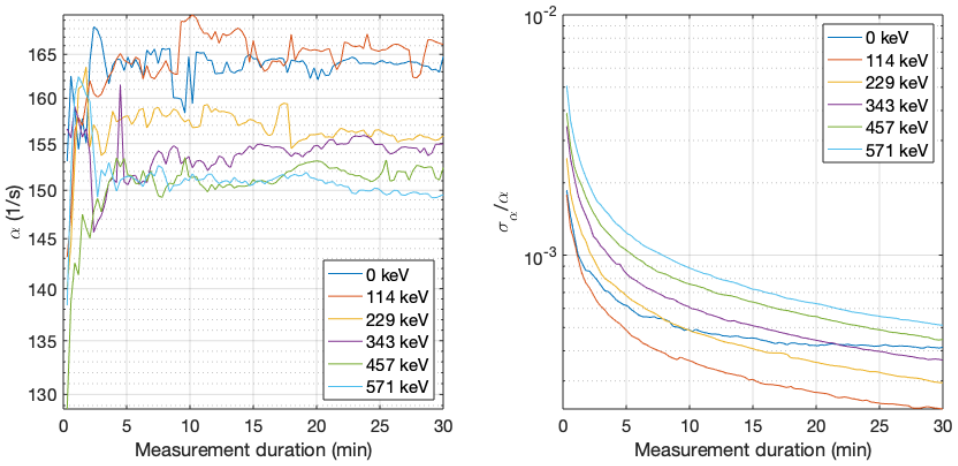

Figure J.3: $CeBr_3$ detectors count rate and CPSD amplitude as function of threshold.

Appendix K

LEAF setup for noise measurements

Table K.1: LEAF signal processing setup.

Detector label	EPFL Serial number (1/s)	Signal output	HV supply	Experimental position
$CeBr_3$ #1	91	DSA 419	DSA 419	CR North
$CeBr_3$ #2	92	DSA 420	DSA 420	CR South
BGO #1	93	DSA 419	DSA 420	South
BGO #2	94	DSA 420	External HV	North
BF_3 #1	8	Amplifier	External HV	Peripheral South
BF_3 #2	6	Amplifier	External HV	Peripheral North

Appendix L

Neutron and Gamma correlation measurements with $CeBr_3$ and BF_3 detectors

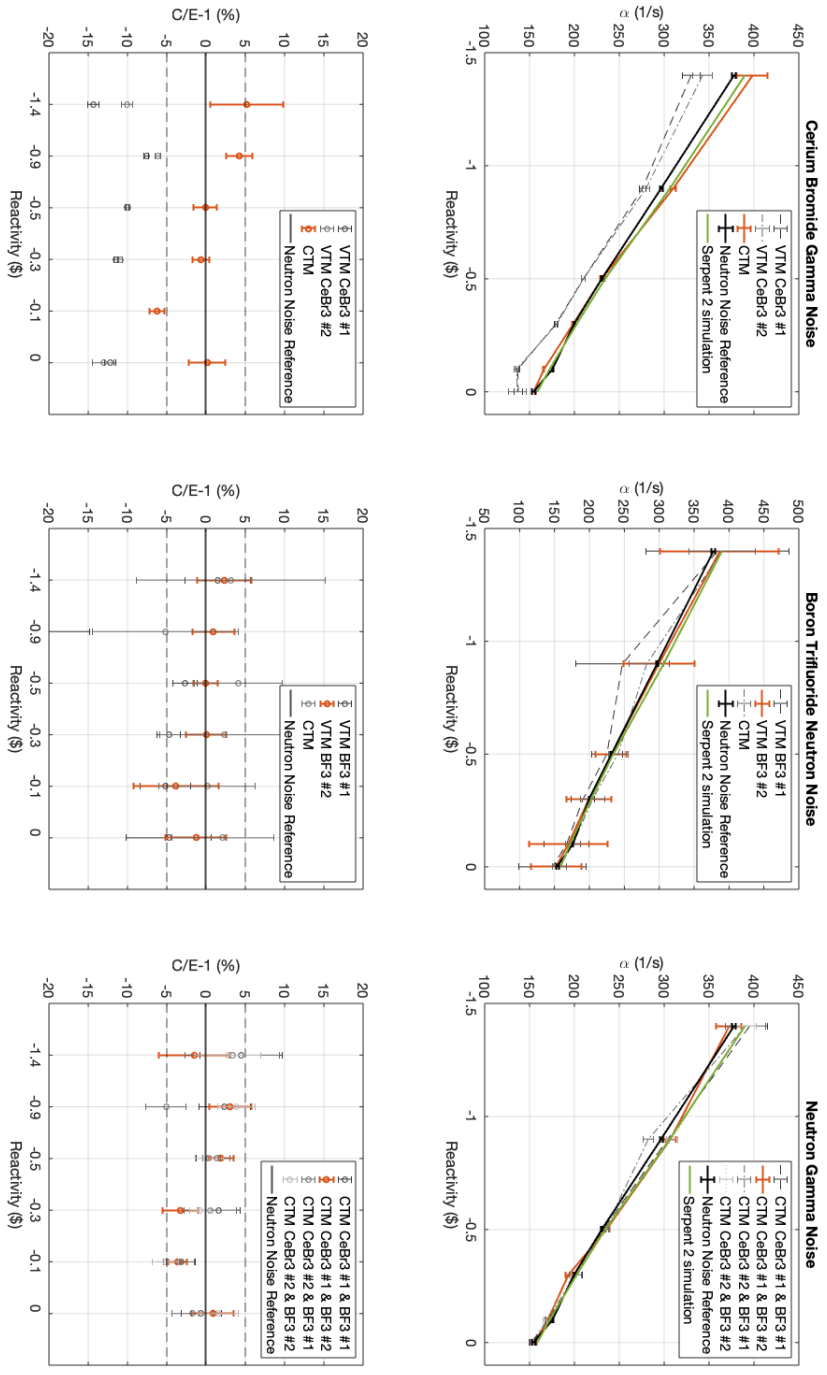

Figure L.1: Prompt gamma decay constant for gamma, neutron and neutron-gamma correlation measurements, obtained with Feynman-α curve fitting.

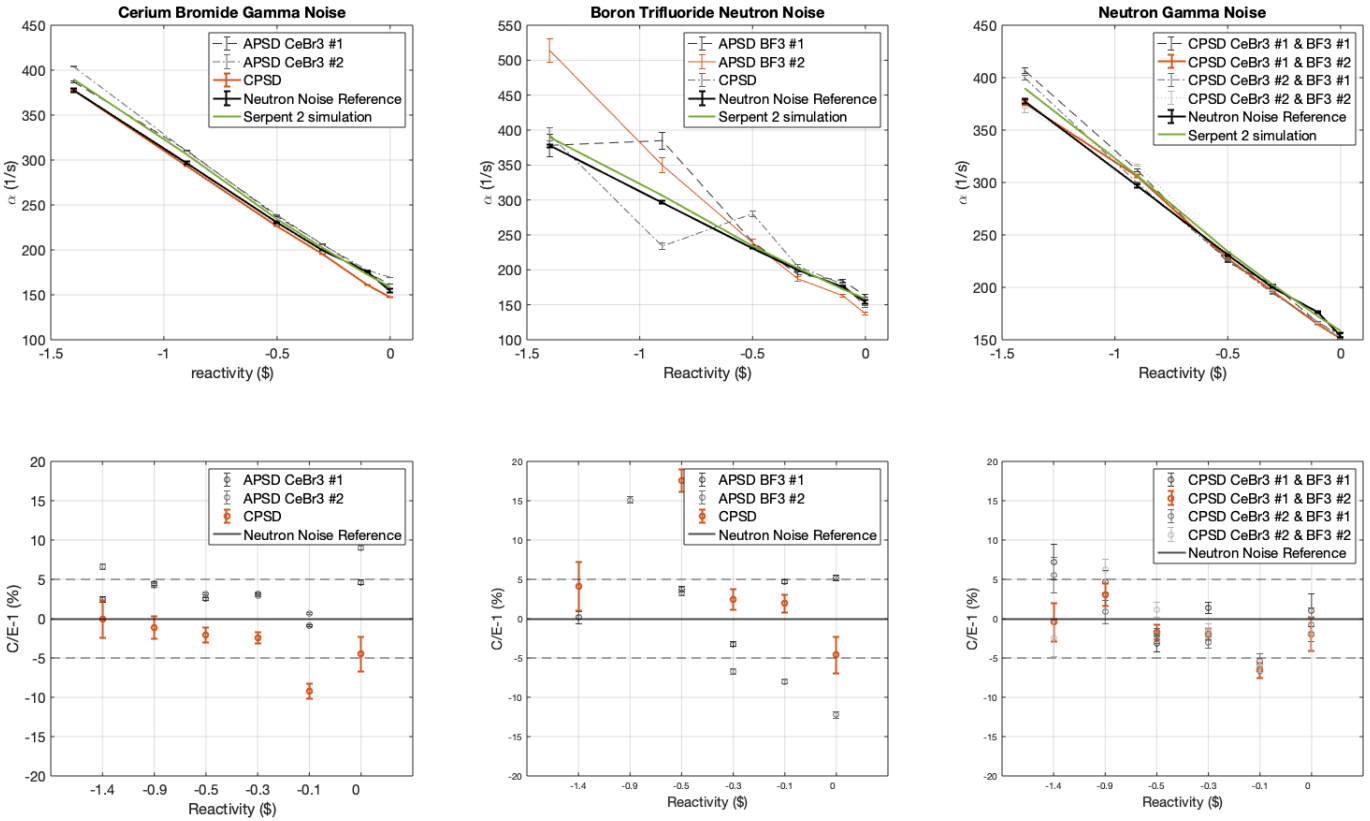

Figure L.2: Prompt gamma decay constant for gamma, neutron and neutron-gamma correlation measurements, obtained with Cohn-α curve fitting.

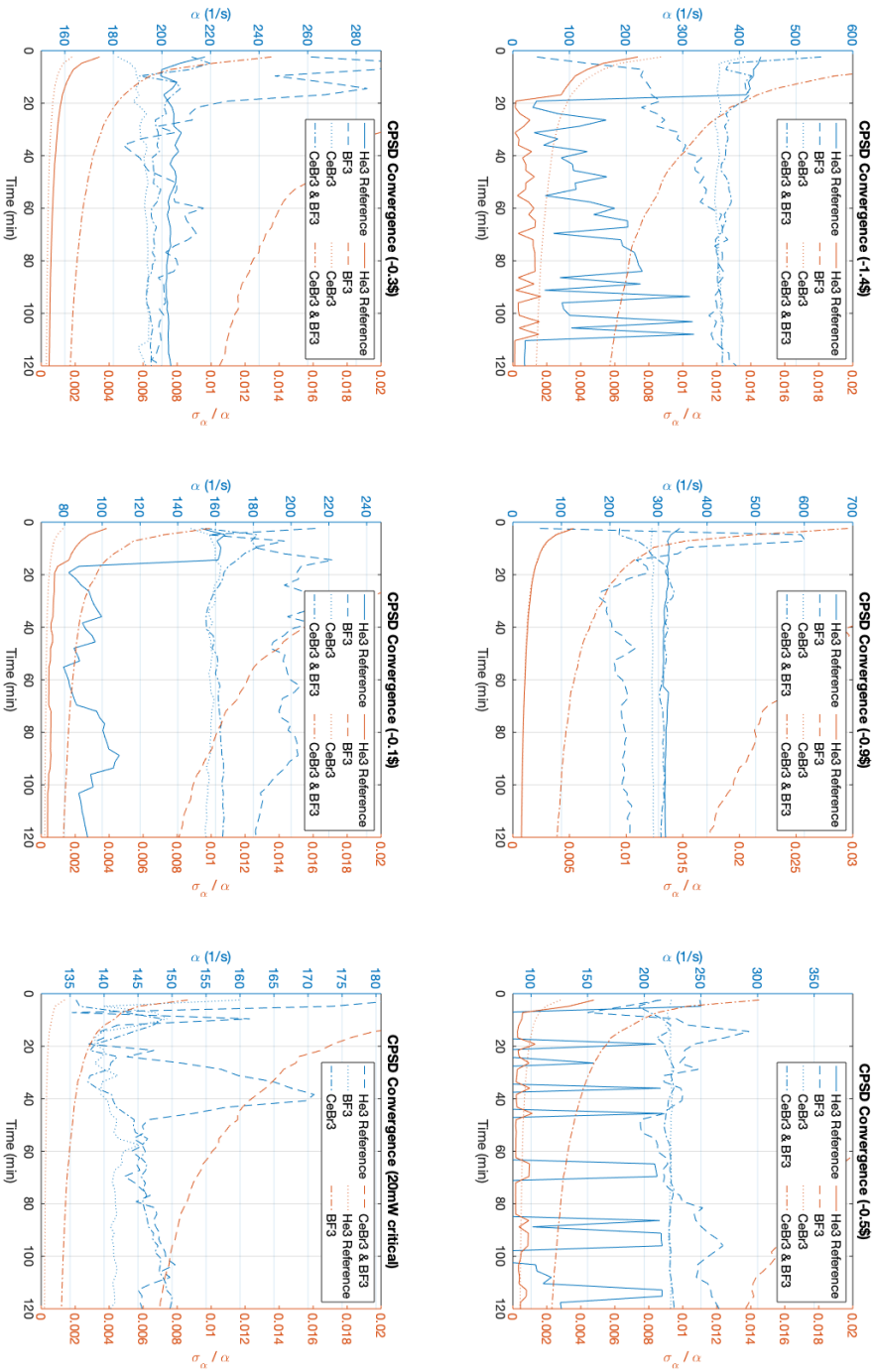

Figure L.3: Prompt gamma decay constant and its relative uncertainty as function of the measurement length, for $CeBr_3$ gamma correlations, BF_3 neutron correlations, neutron-gamma correlations with these very same detectors, and He-3 reference neutron correlations. This was performed for 6 reactivity level from -1.4$ to critical.

Appendix M

Bismuth Germanate distance measurements

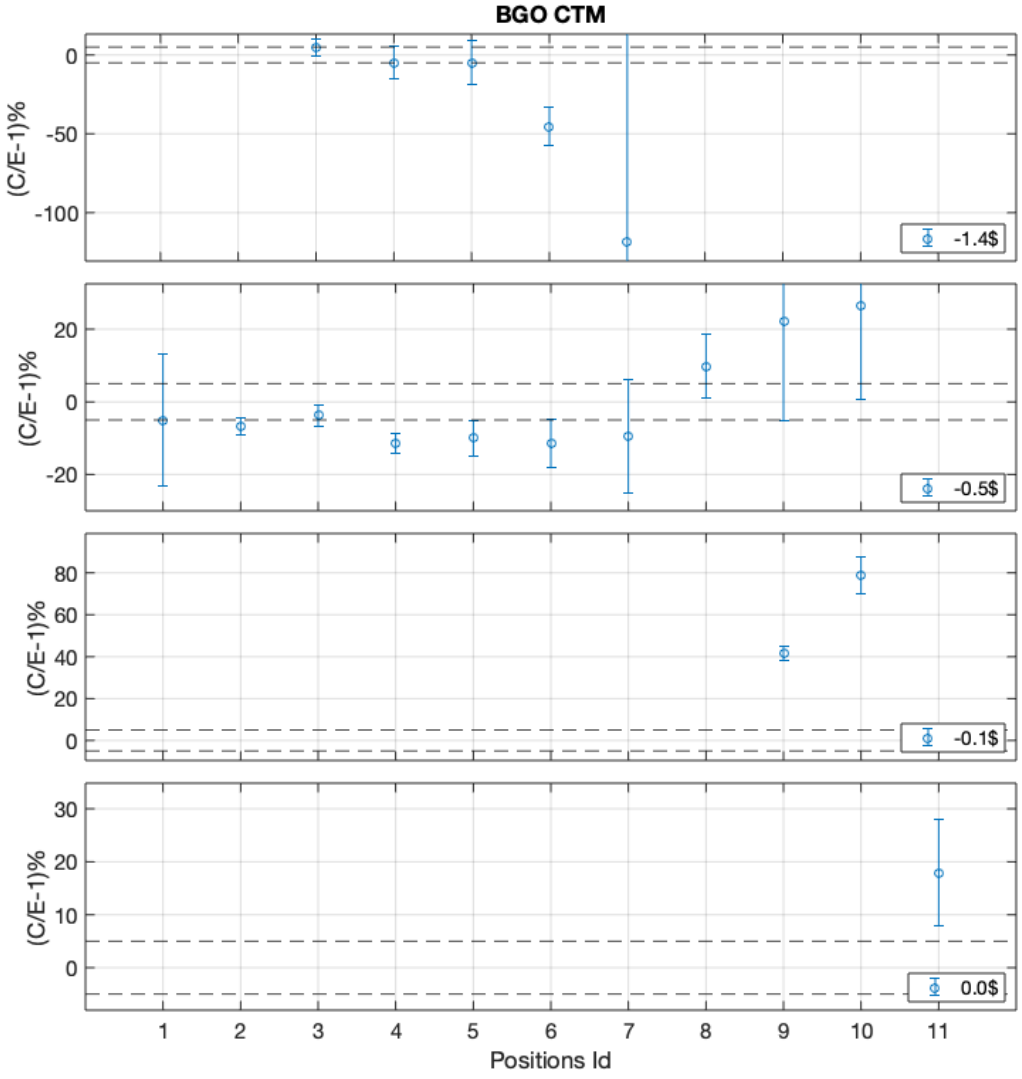

Figure M.1: Prompt gamma decay constant obtained with CTM curve fitting for BGO distance measurements.

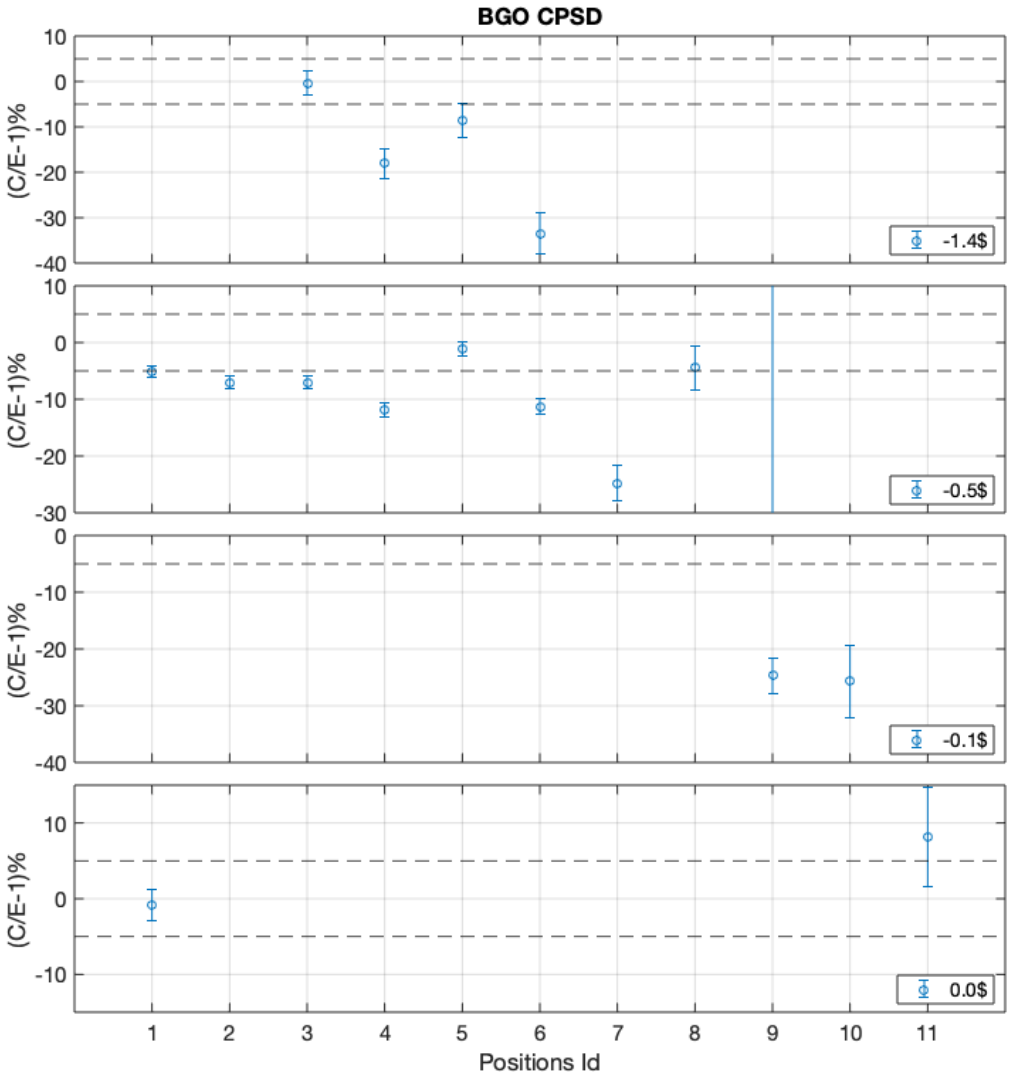

Figure M.2: Prompt gamma decay constant obtained with CPSD curve fitting for BGO distance measurements.

Bibliography

[1] Oskari Pakari. *Experimental and numerical study of stochastic branching noise in nuclear reactors.* PhD thesis, Ecole polytechnique federale de Lausanne (EPFL), 2020.

[2] Gordon R. Gilmore. *Practical Gamma-Ray Spectrometry.* John Wiley & Sons, Ltd, apr 2008.

[3] K.S. Shah, J. Glodo, W. Higgins, E.V.D. van Loef, W.W. Moses, S.E. Derenzo, and M.J. Weber. Cebr3 scintillators for gamma-ray spectroscopy. *IEEE Transactions on Nuclear Science*, 52(6):3157–3159, dec 2005.

[4] Paul Guss, Michael Reed, Ding Yuan, Matthew Cutler, Christopher Contreras, and Denis Beller. Comparison of CeBr 3 with LaBr 3 :ce, LaCl 3 :ce, and NaI:tl detectors. In Arnold Burger, Larry A. Franks, and Ralph B. James, editors, *Hard X-Ray, Gamma-Ray, and Neutron Detector Physics XII*. SPIE, aug 2010.

[5] O. H. Nestor and C. Y. Huang. Bismuth germanate: A high-z gamma-ray and charged particle detector. *IEEE Transactions on Nuclear Science*, 22(1):68–71, 1975.

[6] *DSA-LX, Digital signal analyzer.*

[7] Jaakko Leppanen. Development of a new monte carlo reactor physics code. *978-951-38-7018-8*, 2007.

[8] M White. Development and implementation of photonuclear cross-section data for mutually coupled neutron-photon transport calculations in the monte carlo n-particle (mcnp) radiation transport code. *Los Alamos National Lab. (LANL), Tech. Rep.*, 2000.

[9] *Serpent: a Continuous-Energy Monte Carlo Reactor Physics Burnup Calculation Code, http://serpent.vtt.fi/mediawiki/index.php/ENDF_reactionMT%27s_and_macroscopic_reaction_numbers.*

[10] J. H. Hubbell. Photon mass attenuation and mass energy-absorption coefficients for h, c, n, o, ar, and seven mixtures from 0.1 keV to 20 MeV. *Radiation Research*, 70(1):58, apr 1977.

[11] O. Pakari, V. Lamirand, B. Vandereydt, F. Vitullo, M. Hursin, C. Kong, and A. Pautz. Design and simulation of gamma spectrometry experiments in the CROCUS reactor. *EPJ Web of Conferences*, 225:04016, 2020.

[12] J.M. Verbeke, J. Randrup, and R. Vogt. Fission reaction event yield algorithm FREYA 2.0.2. *Computer Physics Communications*, 222:263–266, jan 2018.

[13] D. Fourmentel, V. Radulovic, L. Barbot, J-F. Villard, G. Zerovnik, L. Snoj, M. Tarchalski, K. Pytel, and F. Malouch. Delayed gamma measurements in different nuclear research reactors bringing out the importance of their contribution in gamma flux calculations. *IEEE Transactions on Nuclear Science*, 63(6):2875–2879, dec 2016.

[14] K. Ambrožič, A. Gruel, V. Radulović, M. Le Guillou, P. Blaise, C. Destouches, and L. Snoj. Delayed gamma determination at the JSI TRIGA reactor by synchronous measurements with fission and ionization chambers. *Nuclear Instruments and Methods in Physics Research Section A: Accelerators, Spectrometers, Detectors and Associated Equipment*, 911:94–103, dec 2018.

[15] Oskari Pakari, Vincent Lamirand, Gregory Perret, Daniel Godat, Mathieu Hursin, Pavel Frajtag, and Andreas Pautz. Investigation of spatial effects on neutron noise measurements in the zero power reactor crocus. In *PHYSOR 2018: Reactor physics paving the way towards more efficient systems, At Cancun, Mexico*, 2018.

[16] Bruno Bärs. Reactor gamma noise studies. *Annals of Nuclear Energy*, 2(2-5):107–118, 1975.

[17] Bruno Bärs. On the use and influence of gamma radiation in reactor noise measurements. *Nuclear Technology*, 30(1):12–23, 1976.

[18] K. Hashimoto, S. Yamada, Y. Hasegawa, and T. Horiguchi. Feynman-α correlation analysis by prompt-photon detection. *Annals of Nuclear Energy*, 25(1-3):13–22, 1998.

[19] John R. Lamarsh. *Introduction to Nuclear Reactor Theory*. Addison-Wesley, 1972.

[20] Vincent Lamirand, Pavel Frajtag, Daniel Godat, Oskari Pakari, Axel Laureau, Adolfo Rais, Mathieu Hursin, Grégory Hursin, Carlo Fiorina, and Andreas Pautz. The COLIBRI experimental program in the CROCUS reactor: characterization of the fuel rods oscillator. *EPJ Web of Conferences*, 225:04020, 2020.

[21] Dina Chernikova, Kåre Axell, Senada Avdic, Imre Pázsit, Anders Nordlund, and Stefan Allard. The neutron–gamma feynman variance to mean approach: Gamma detection and total neutron–gamma detection (theory and practice). *Nuclear Instruments and Methods in Physics Research Section A: Accelerators, Spectrometers, Detectors and Associated Equipment*, 782:47–55, may 2015.

[22] R. L. Plackett. Some theorems in least squares. *Biometrika*, 37(1/2):149, jun 1950.

[23] V.G. Dovì, O. Paladino, and A.P. Reverberi. Some remarks on the use of the inverse hessian matrix of the likelihood function in the estimation of statistical properties of parameters. *Applied Mathematics Letters*, 4(1):87–90, 1991.

[24] Bradley Efron. Better bootstrap confidence intervals. *Journal of the American Statistical Association*, 82(397):171–185, mar 1987.

[25] O.Petit A.Zoia V.Lamirand A.Pautz O.Pakari, D.Mancusi. Towards the validation of noise experiments in the crocus reactor using the tripoli-4 monte carlo code in analog mode. In *PHYSOR 2020: Transition to a Scalable Nuclear Future*, 2020.

[26] M. Gierlik, T. Batsch, M. Moszynski, T. Szczesniak, D. Wolski, W. Klamra, B. Perot, and G. Perret. Comparative study of large NaI(tl) and BGO scintillators for the EURopean illicit TRAfficking countermeasures kit project. In *IEEE Nuclear Science Symposium Conference Record*. IEEE, 2005.

[27] F.G.A. Quarati, P. Dorenbos, J. van der Biezen, Alan Owens, M. Selle, L. Parthier, and P. Schotanus. Scintillation and detection characteristics of high-sensitivity cebr3 gamma-ray spectrometers. *Nuclear Instruments and Methods in Physics Research Section A: Accelerators, Spectrometers, Detectors and Associated Equipment*, 729:596–604, nov 2013.

[28] *High resolution Cebr3 scintillators, Datasheet, https://www.berkeleynucleonics.com/sites/default/files/products/datasheets/cebr3_ datasheet_ 2017.pdf.*

[29] *High density BGO scintillators, Datasheet, https://www.crystals.saint-gobain.com/sites/imdf.crystals.com/files/documents/bgo-material-data-sheet.pdf.*

[30] Vincent Lamirand, Axel Laureau, Dimitri Rochman, Gregory Perret, Adrien Gruel, Pierre Leconte, Patrick Blaise, and Andreas Pautz. An experimental programme optimized with uncertainty propagation: PETALE in the CROCUS reactor. *EPJ Web of Conferences*, 211:03003, 2019.

[31] IAEA. *Database of Prompt Gamma Rays from Slow Neutron Capture for Elemental Analysis*. INTERNATIONAL ATOMIC ENERGY AGENCY, 2007.

[32] *Cuve d'eau CARROUSEL, https://www.epfl.ch/labs/lrs/fr/page-130375-fr-html/page-132446-fr-html/.*

Acknowledgments

This thesis could not have been realised without the help of numerous people around me. The last page of this work is therefore devoted to thanking these people.

A first recognition goes to Prof. Andreas Pautz who gave me the chance to work in this very inspiring environment.

I would like to express my gratitude to my supervisors Dr. Vincent Lamirand and Oskari Pakari. Both of them invested valuable time to assist me with my project and, besides their sound advice and critique, working at their side helped me thrive professionally.

I would also like to thank Dr, Axel Laureau for his efforts assisting me with Python and for his informed opinion on all my interrogations.

For the pleasant moments in the daily life of the lab, I thank Dr. Mathieu Hursin, Dr. Carlo Fiorina, Dr. Pavel Frajtag, Laurent Braun and Daniel Godat, Stefan Radman, Fanny Vitullo and Alessandro Scolaro. The thrilling environment boosted my motivation and made the project time so pleasant.